

The relationship between depth, age and gravity in the oceans

A. G. Crosby,¹ D. McKenzie¹ and J. G. Sclater²

¹*Bullard Laboratories of the Department of Earth Sciences, University of Cambridge, CB3 0EZ, UK. E-mail: crosby@madingley.org*

²*Scripps Institution of Oceanography, University of California San Diego, La Jolla, CA 92037, USA*

Accepted 2006 March 17. Received 2006 March 17; in original form 2005 October 11

SUMMARY

We reassess the applicability of the thermal plate cooling model to the subsidence of the North Pacific, Atlantic and North Indian Ocean Basins. We use a new numerical plate model in which the thermophysical parameters of the lithosphere vary with temperature according to the results of laboratory experiments, and the ridge temperature structure is consistent with the thickness of the oceanic crust. We first attempt to exclude thickened crust from our data set, and then to exclude swells and downwellings by masking regions of the data that remains that have significant gravity anomalies when there exists a clear regional correlation between intermediate-wavelength gravity and topography. We find that the average variation of depth with age is consistent with conventional half-space models until about 90 Myr. Thereafter, the departure from the half-space cooling curve is more rapid than predicted using simple conductive plate cooling models. The depth–age curves in the Pacific and Atlantic show ~250 m of temporary shallowing between the ages of 90–130 Myr, a result consistent with the outcome of experiments on the initiation of small-scale boundary layer convection. The results do not change significantly if the estimated component of the gravity arising from plate cooling is subtracted prior to calculation of the correlation between gravity and topography. A 90-km-thick conductive plate is nevertheless a reasonable model for the average temperature structure of the oldest part of the Pacific ocean lithosphere. In the Pacific, the broad topographic undulations associated with the Line Island Swell, the Hawaiian Swell and surrounding basins have correlated gravity anomalies and an admittance of approximately 30 mGal km⁻¹ and are likely to result from convective circulation in the upper mantle. In the Northeast Atlantic, the intermediate-wavelength admittance over the Cape Verde swell is similar; in the Northwest Atlantic over the Bermuda Swell it is slightly larger but not as well constrained.

Key words: free-air gravity, mantle convection, oceanic lithosphere, thermal subsidence, topography.

1 INTRODUCTION

The primary means by which the Earth loses heat is by plate creation at ridges. As hot rock moves away from the site of upwelling at the ridge it cools from contact with the sea, becomes more dense, and subsides. The simplest thermal model of the ocean lithosphere is a half space, initially at constant temperature, that cools from the top by conduction. The isostatic subsidence of such a half space is proportional to the square root of the time elapsed since it started cooling (in other words, a plot of depth versus the square root of age is a straight line). Davis & Lister (1974), using data from Sclater *et al.* (1971), showed that the average depth of the central eastern Pacific is remarkably consistent with the half space cooling model up to an age of at least 80 Myr. However, Sclater *et al.* (1975) and Parsons & Sclater (1977) examined the relationship between sediment-corrected depth and age in the North Pacific and North Atlantic for selected areas of the ocean floor aged between 120 and

160 Myr, and found that the depth is everywhere significantly shallower than predicted by the half space model. They instead showed that the average subsidence and heat flow could be fitted using a model of a cooling conductive plate with a constant lower boundary temperature. The model which best-fitted the data available had a plate thickness of 125 km and a basal temperature of 1330°C. Parsons & McKenzie (1978) suggested that the flattening is caused by the addition of heat to the lithosphere after the onset of instability in the thermal boundary layer underneath the mechanical lid.

By using a plate model to understand the isostatic subsidence of old seafloor, Parsons & Sclater (1977) assumed that the average vertically-integrated density difference between the lithosphere at a given age and the ridge was the same as if the lithosphere were a rigid conductive plate with a constant basal temperature. Numerical studies of convection in a 2-D box by Richter & McKenzie (1981) confirmed that the assumption is reasonable if the lithosphere is in steady state. We define the base of the thermal lithosphere to be the

Here, we argue that it is only possible to test the plate model once the effects of both anomalous volcanism and mantle convection on the average topography have been accounted for. We make use of recently published grids of satellite-derived sea-surface gravity anomalies and predicted seafloor topography to identify regions of anomalous crust, flexure and dynamic topography. We then exclude these regions and attempt to establish the average variation of unperturbed seafloor depth with age in the North Pacific, North Indian and Northwest, Northeast and Southeast Atlantic ocean basins. Interestingly, the general procedure we follow was first suggested more than 30 years ago by Sclater *et al.* (1975), but has not been used since, perhaps because the marine gravity field was poorly known until relatively recently.

In summary, our method is as follows. We first eliminate topographic measurements over plateaus, seamounts, flexural moats, and major fracture zones from our data set by eye, and make an isostatic correction for loading by sediments. We then separate age-related and dynamic depth variation by dividing the remaining data into narrow age bins, and within each plot gravity against topography. We do this to assess the extent to which gravity and topography are correlated away from sites of anomalous crust. When the observed correlation is significant, we estimate the gravity–topography ratio, which is useful for, amongst other things, constraining the thickness of the mechanical boundary layer (e.g. McKenzie 1994). Having investigated the correlation, we then exclude both positive and negative dynamic topography from our data set by eliminating regions with gravity anomalies larger than a certain magnitude. We initially assume that all of the regions with no gravity anomalies are unperturbed, and the gravity anomalies result from mantle processes with a longer wavelength than the instabilities underneath the cooling plate. Finally, we plot the remaining topographic measurements against crustal age, and compare the results with the predictions of an updated and more realistic conductive plate model, discussed extensively by McKenzie *et al.* (2005). We then conclude by examining how residuals about the average depth–age trend vary as a function of position.

2 SOURCES OF DATA

2.1 Topography, gravity and age

We only used depth measurements that have been constrained by bathymetric sounding. Our starting point was the 2 min grid of Smith & Sandwell (1997), which is a synthesis of shipboard measurements and topography predicted from the sea-surface gravity field. The authors ensured that in blocks where there was real data, the model and the data agreed. They also made some effort to exclude bad tracks beforehand. It is an artificial property of the data set (and one which introduces a maximum error of 1 m) that only cells in the grid that are constrained by sounding have depths that are odd integers, and we used only those cells. The surface gravity field we use is described by Sandwell & Smith (1997), and the crustal age grid by Müller *et al.* (1997).

2.2 Sediment thickness and density

The grid we use for the Pacific and Indian oceans is part of a global marine sediment thickness map compiled by David Divins of NGDC (Divins 2004, and references therein). In the Northwest Atlantic, we combined Divins' grid and a more recent grid made by Loudon *et al.* (2004). Away from the continental margin, both authors have incor-

porated the sediment thickness map of Tucholke *et al.* (1982); we have been unable to find any more recent compilations. To constrain sediment density, we used the Lamont-Doherty Earth Observatory online catalogue of measurements, recorded *in situ* using the Hostile Environment Litho-density Sonde during Ocean Drilling Program (ODP) and Deep Sea Drilling Program (DSDP) cruises.

3 DATA PROCESSING

3.1 Exclusion of thickened crust and subduction zones

We used the topographic map of Smith & Sandwell (1997) to mark and then digitize a set of polygons around subduction zones and areas of thickened crust, and then applied standard computer codes to exclude depth measurements located inside them. Figs 2 and 3 show the polygons and the topography that remained. Constructing polygons is necessarily a subjective process: for areas of thickened crust we used the review of Coffin & Eldholm (1994) to identify areas that had experienced anomalous volcanism, and the 5 km isobath as a rough guide to the edge of each edifice which occurs on old ocean floor. In the Pacific, we also excluded data from the Emperor and Chinook troughs to the east of the Emperor seamounts. The troughs are anomalously deep and may be either fossil fracture zones (Farrar & Dixon 1981) or abandoned rift centres (Rea & Dixon 1983; Mammerickx & Sharman 1988). When excluding subduction zones, the polygon boundary nearest the ridge was placed at the edge of the flexural bulge, which is clearly visible in the sea-surface gravity field.

Our choice of subjective methods to exclude regions of thickened crust is deliberate. Although automated methods (e.g. Hillier & Watts 2005) have the advantages of being objective and reproducible, they use much simpler criteria than a human interpreter, who can easily take into account a large number of factors in deciding whether a region is anomalous.

3.2 Exclusion of flexural moats and major fracture zones

Although most flexural moats around seamounts are filled with sediment and are not apparent in the topography, they are associated with clear negative gravity anomalies that are unrelated to deeper mantle processes. The same is true for major fracture zones. We used the gravity of Sandwell & Smith (1997) to define an additional set of polygons enclosing moats and major fracture zones which have gravity anomalies that are clearly larger than the variance of the background seafloor fabric, and excluded the topography within each polygon from our data set. The masks are shown in Figs 4 and 5, and to an extent overlap the masks in Figs 2 and 3.

3.3 Application of a 30 min block median

After masking the anomalous regions discussed in the previous sections, we obtained 30 min block-medians of the topography and gravity at the remaining data points in order to obtain a more geographically even data coverage.

3.4 Isostatic loading corrections

We then applied a simple isostatic sediment correction by balancing the weight per unit cross sectional area of loaded and unloaded

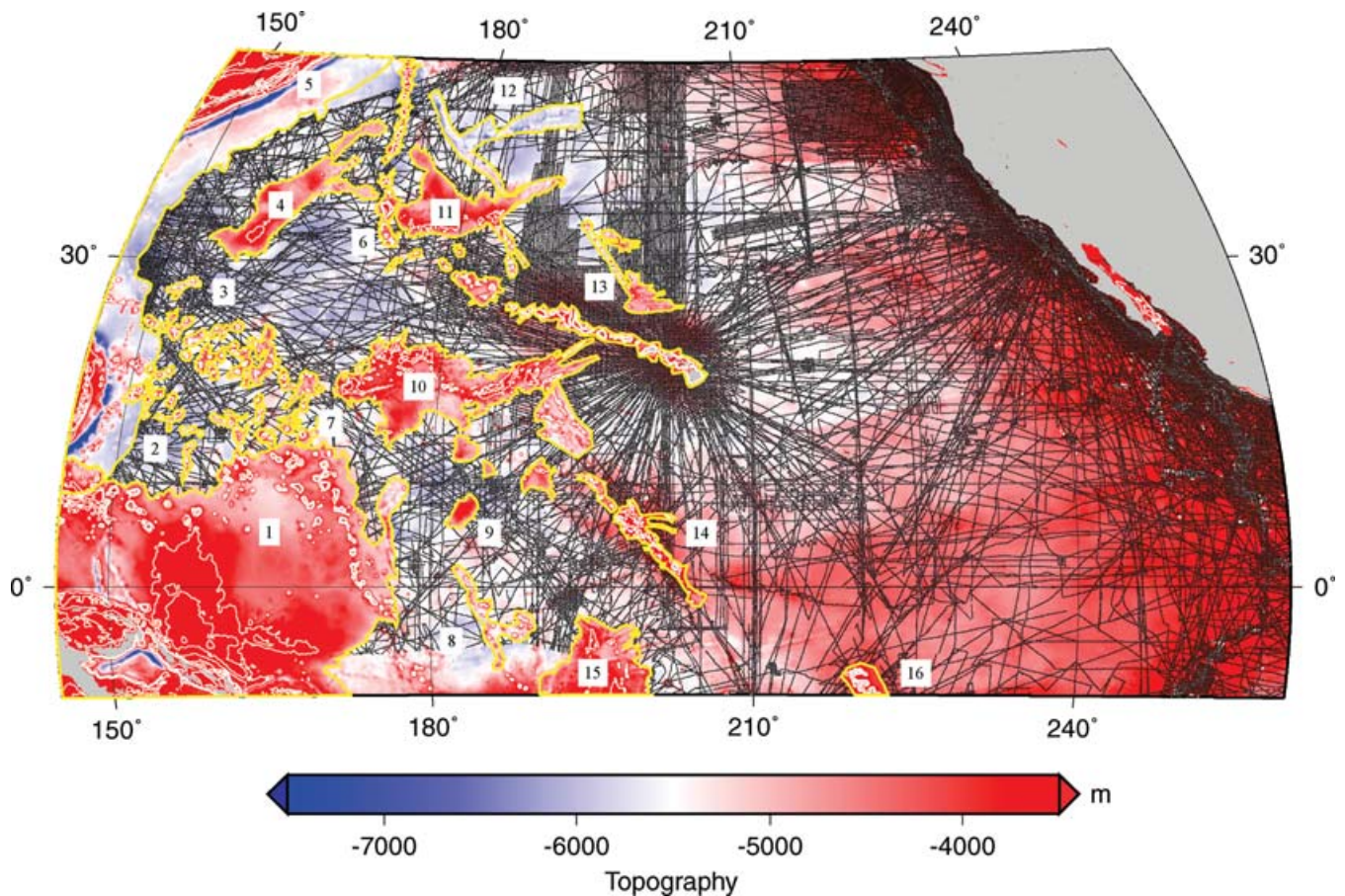


Figure 2. Topography in the North Pacific ocean. The underlying colour grid is the model of Smith & Sandwell (1997). White lines are -3 , -2 , and -1 km topographic contours, and black lines are regions where the topography has been constrained by shipboard sounding and where the age of the crust is given by Müller *et al.* (1997). Yellow polygons enclose anomalous regions identified by eye in which the topography was excluded. 1: Ontong Java, Caroline Islands, Eauripik Rise, Nauru Basin, Marshall-Gilbert Seamounts. 2: Magellan seamounts. 3: Marcus-Wake and Japanese Seamounts. 4: Shatsky Rise. 5: Mariana, Kuril, and Japan trenches and associated flexural bulges. 6: Emperor Seamounts. 7: Northern Marshall Seamounts. 8: Tokelau and Phoenix Islands. 9: Magellan Rise. 10: mid-Pacific Mountains. 11: Hess Rise. 12: Chinook and Emperor Troughs. 13: Hawaiian Ridge and Musicians' Seamounts. 14: Line Islands. 15: Manihiki Plateau. 16: Marquesas Islands.

lithospheric columns. The correction is

$$\Delta z = \frac{\rho_m t_s - q}{\rho_m - \rho_w}, \quad (1)$$

where ρ_m is the density of the mantle (3300 kg m^{-3}) and ρ_w the density of water. q is the mass per unit cross-sectional area of the sediment column and t_s is the total sediment thickness.

The Pacific was divided into four regions listed in Table 1. In each of them we assumed a simple constant or linear relationship between depth and density based on ODP logs. The sediment correction throughout the Pacific is usually less than a few hundred metres.

However, the sediment cover in the Atlantic is thicker, especially over the oldest ocean floor that bounds the continental margin. *In situ* sediment density data away from the margin are sparse and variable, so we applied two different sediment corrections in order to understand the extent to which we could be confident of the unloaded topography. The first uses a linear burial depth–density model (based on a rough average of ODP logs 418, 950, 952, 994, 995, 1051, 1052, 1061, 1062, 1063, 1263 and 1265), in which the sediment has a density of 1.75 Mg m^{-3} at a depth of 250 m and a density of 2.0 Mg m^{-3} at a depth of 700 m, with the added constraint that the sediment density cannot exceed 2.8 Mg m^{-3} . The second, after Loudon *et al.* (2004), involves converting thickness to two-way seis-

mic travel-time, and then applying a standard correction described by Crough (1983). This approach does not make use of eq. (1) directly.

In the Indian ocean, the sediment cover is mostly thin clays. Therefore, we applied the same correction as in the deep Pacific away from seamounts and the equatorial high productivity zone.

Finally, on the basis of ODP sampling and multi-channel seismic reflection data, Abrams *et al.* (1993) argue that the original Mesozoic oceanic crust in the East Mariana and Pigafetta basins is covered by approximately 100–400 m of Cretaceous lava flows. An isostatic correction for these was applied using Fig. 9(b) in Renkin & Sclater (1988). In theory, one could make a similar correction for all the other areas of thickened crust; however, the uncertainties in their thickness and density are such that it is better to simply exclude them from the data set, as we have already done.

3.5 Residual gravity

The change in the density structure of the lithosphere as it cools and moves away from the ridge gives rise to a gravity anomaly, which is unrelated to the planform of convection under the plate (Lambeck 1972; Cochran & Talwani 1977). Therefore, it is desirable to remove this contribution before plotting gravity against topography as a

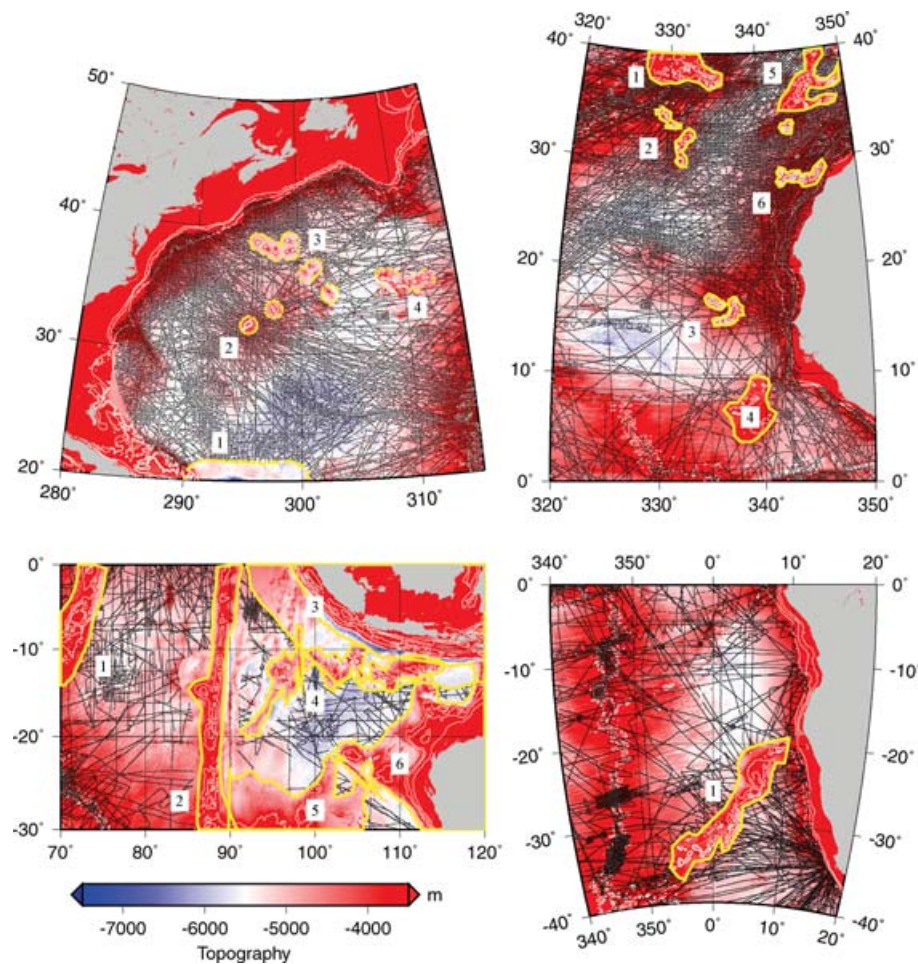


Figure 3. Topography in the Atlantic and Indian oceans. Top left. Northwest Atlantic. 1: Puerto Rico trench and bulge. 2: Bermuda. 3: New England Seamounts. 4: Corner Seamounts. Top right. Northeast Atlantic. 1: Azores. 2: Cruiser and Great Meteor Seamounts. 3: Cape Verde. 4: Sierra Leone Rise. 5: Madeira and Horseshoe Seamounts. 6: Canary Islands. Bottom Left. North Indian Ocean. 1: Chagos-Laccadive Ridge. 2: Ninetyeast Ridge. 3: Java and Sunda trenches and bulges. 4: Vening-Meinesz Seamounts, Roo Rise, Cocos-Keeling Islands. 5: Broken Plateau. 6: Cuvier and Exmouth Plateaus. Bottom Right. Southeast Atlantic. 1: Walvis Ridge.

function of age. An approximate method of calculating the plate gravity is outlined in Appendix B. We define *residual gravity* as the observed gravity from which the calculated plate gravity has been subtracted. Because the calculated plate gravity is only an approximation, we work with both observed and residual gravity throughout the rest of this paper.

3.6 Exclusion of dynamic topography

To separate age-related and dynamic depth variation we divided the processed data into 10 Myr bins, and within each plotted the 30 min block-medians of the depth against both gravity and residual gravity (see Fig. 6 for an example). We then excluded blocks with significant positive gravity anomalies (swells) or significant negative gravity anomalies (troughs). In the Pacific, we kept only blocks in which the median gravity anomaly is between -5 and $+5$ mGal; in the Atlantic and Indian oceans, where there are fewer data, our pass range was -10 to $+10$ mGal. However, we used all the data to estimate the best-fitting linear relationship between gravity and topography, and the method of Marks & Sandwell (1991), which minimizes residuals in both the topography and gravity. In order to assess the quality of the correlation, we also calculated Spearman's Rank Correlation Coefficient (r_s). Finally, for ocean floor younger than a certain threshold (indicated in the results) we used all the topog-

raphy in each age band to calculate the average depth, because the accuracy of the calculated plate gravity is uncertain near the ridge.

3.7 Reference depth–age curves

A reference depth–age table for an ocean basin should describe the average variation of depth with age in the absence of sediments, anomalous volcanism, or dynamic topography. We calculated the three quartiles of the topography which had not been excluded in each age bin, but discarded bins in which we judged the data to be unreliable. We then constructed reference depth–age curves by interpolating between the remaining median depths in the table. For each bin, the representative age was taken to be at the centre of the time interval.

4 RESULTS

4.1 Reference depth–age curves

4.1.1 North Pacific

Reference depth–age curves for the North Pacific are shown in Figs 6 and 7, with full results listed in Tables A1 and A2. For ocean floor younger than 80 Myr the average subsidence is proportional to the

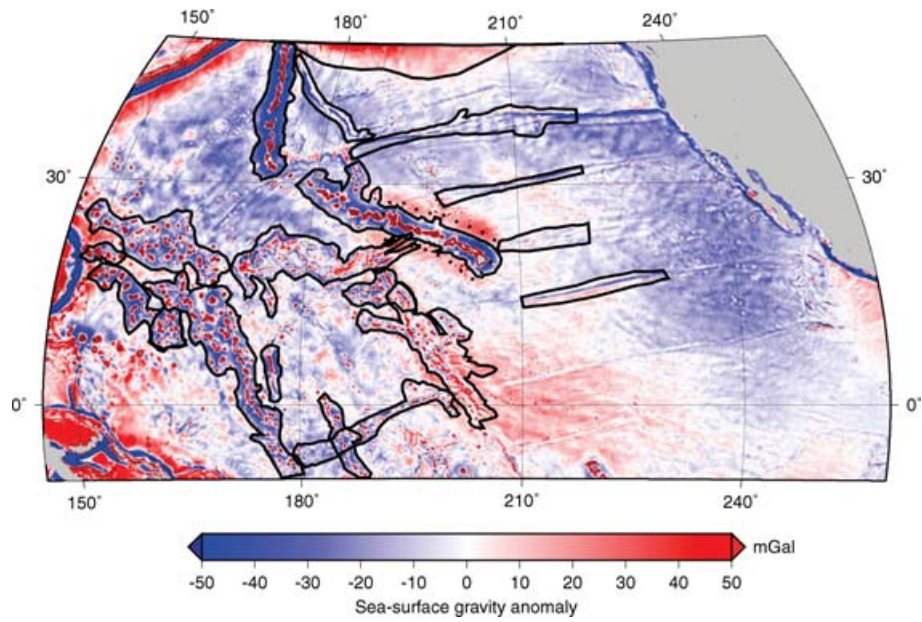


Figure 4. Gravity anomalies in the North Pacific ocean from Sandwell & Smith (1997). The black polygons are further regions in which the topography was excluded. The black dotted line encloses one more region in which the topography was excluded: the edge of the Hawaiian flexural moat has near-zero gravity anomalies but is clearly not on unperturbed seafloor. Contours are every 100 mGal (except zero).

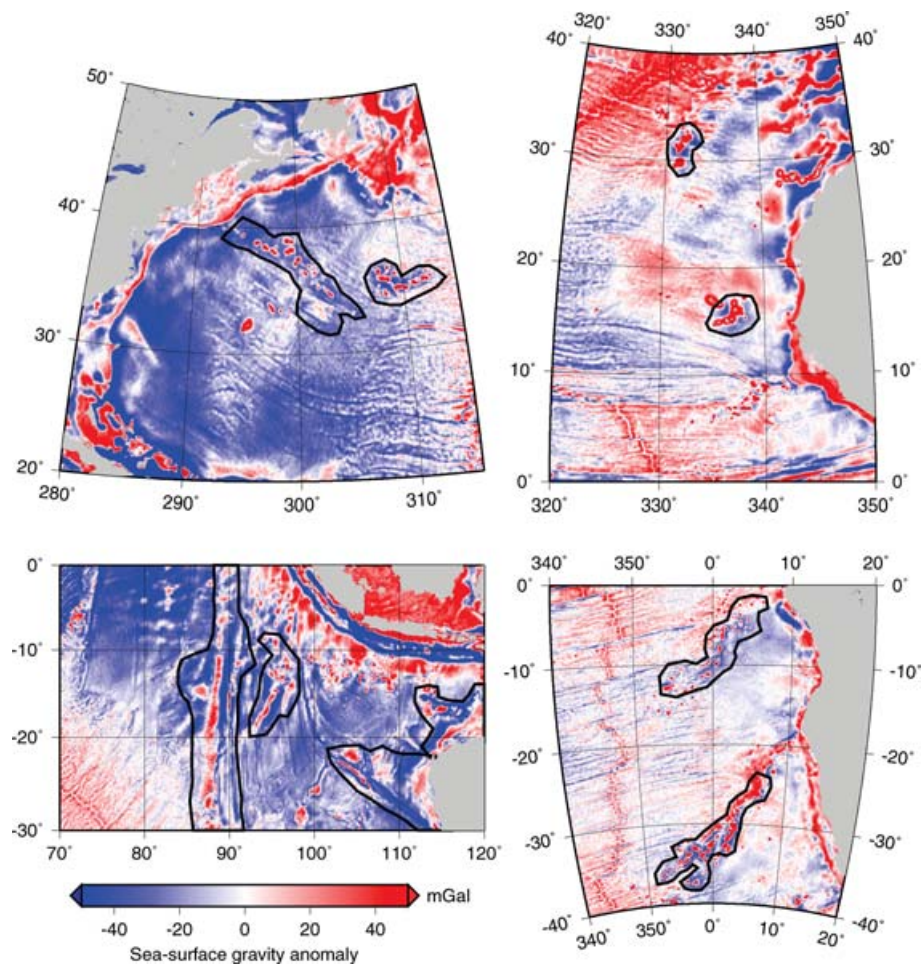


Figure 5. Gravity in the Atlantic and North Indian oceans. Key as in Fig. 4.

Table 1. Sediment regions in the Pacific. Densities are in Mg m^{-3} .

Region	Dominant lithology	ODP controls	Density at 100 m depth	Density at 400 m depth
Equatorial high productivity zone	Biogenic remains	849–850	1.6	1.6
Western seamount province	Volcaniclastic	800–802	1.9	1.9
Deep ocean floor	Clays overlying chert	843, 1149, 1179	1.5	2.5
Young ocean floor	Thin sediments	-	1.6	1.6

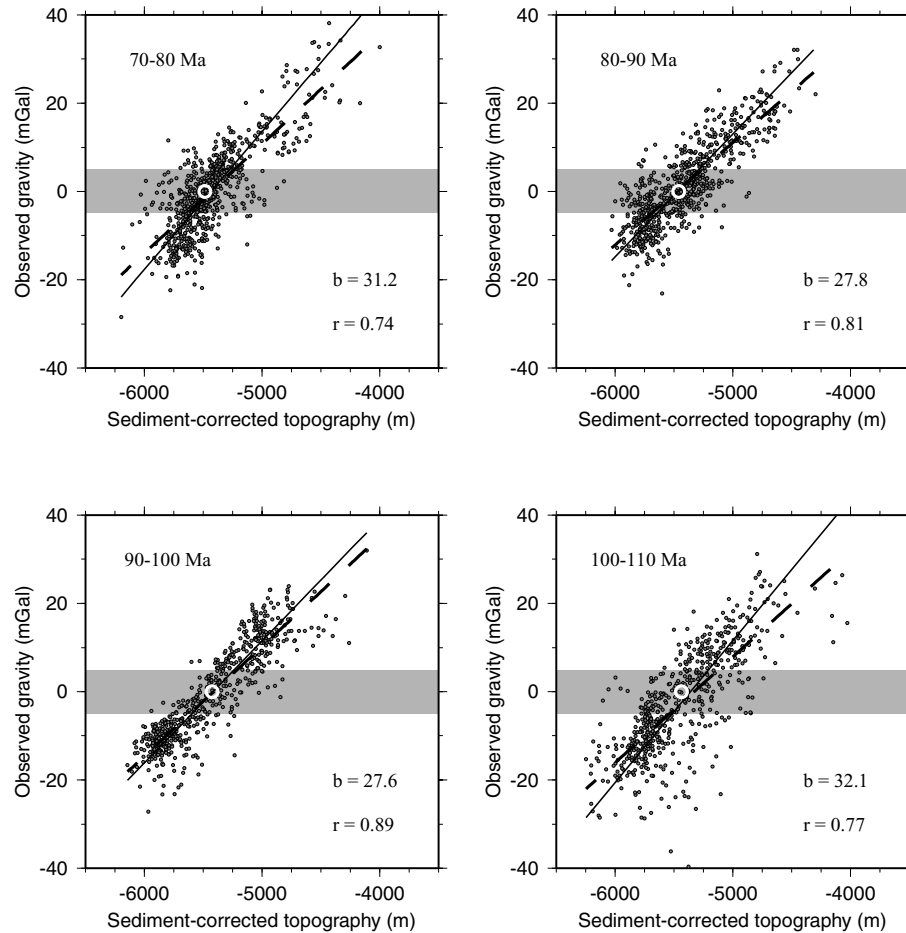


Figure 6. Example plots of observed gravity versus sediment-corrected topography in the north and equatorial Pacific after removal of data over seamounts, plateaus, subduction zones, certain fracture zones and flexural moats, and the calculation of 30 min block medians. Regions with positive gravity anomalies are mainly swells, those with negative gravity anomalies mainly troughs. The shaded grey region shows the data postulated to be over undisturbed seafloor, that is, the data with small gravity anomalies. The solid line is the best-fit straight line estimated using the method of Marks & Sandwell (1991) (MS). The dashed line is calculated using conventional linear regression (in which the error is presumed to be contained entirely within the gravity). The MS slope b (in mGal km^{-1}) and Spearman's Rank Correlation Coefficient r are marked on each plot. The white circle is the median depth of blocks that are plotted in the grey band and is plotted in Fig. 7(a). Full results for the Pacific are given in Tables A1 and A2.

square root of age, as predicted by the classical half-space cooling model (a least-squares fit to the median depths in Fig. 7(b) younger than 90 Ma gives the depth $d = -2821 - 315\sqrt{t}$). The reference depth–age curves in Fig. 7 show that the departure from \sqrt{t} cooling is more sudden than can be explained using *any* plate cooling model. Fig. 7(b) in fact shows ~ 200 m of temporary shallowing between the ages of 90–130 Ma. Interestingly, Levitt & Sandwell (1995) plotted the depth to trench nodes as a function of age and observed a similar bump. However, they suspected that it was a result of sediment accumulation, but did not test their suggestion. If we have failed to exclude the full extent of thickened crust associated with Early Cretaceous plateau formation, the depths in the range 130–150 Ma will be too shallow. Because of uncertainty of the bounds of post-

ridge volcanism and associated flexural and sedimentary features on the oldest ocean floor, we terminated the reference depth–age table at 160 Ma. The reference depth–age curves constructed using the observed and residual gravity fields are similar, which is expected given the rapid spreading rate in the Pacific.

The average depth that our selected part of the seafloor would finally reach as it ages is not well determined, but appears to be between 5750–6000 m. In the absence of a well-constrained asymptotic depth, the age at which subsidence departs from the \sqrt{t} trend can be used to estimate the thermal plate model thickness. The \sqrt{t} part of curve 7B is best fit by eye using a zero-age depth of approximately 2800 m and a plate thickness of 90 km, which is consistent with our extrapolated steady-state depth. Fig. 8 shows our

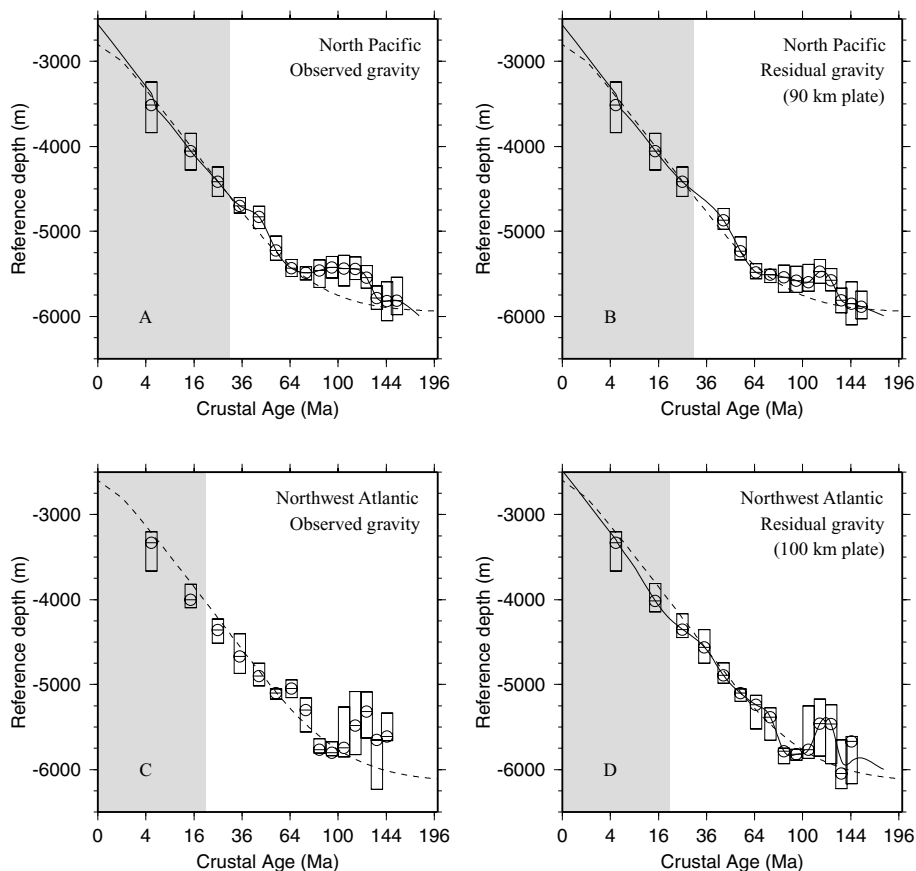


Figure 7. Reference depth versus the square root of age in the Pacific and Northwest Atlantic. The top and bottom of the boxes around the median points are the lower and upper quartiles of the input data, respectively, plotted at the centre of each age band (i.e. 50 per cent of the data lie in the boxes). The observed gravity was used to select the depth values used in figures (a) and (c), and the residual gravity for figures (b) and (d). The solid line is the spline fit, continued at each end of the table. The dashed line is the predicted plate subsidence for a 90 km plate (Pacific) and a 100 km plate (Atlantic). The grey region is young ocean floor, on which all the data was used to evaluate the depth quartiles. For all the oceans apart from the Pacific, the threshold was chosen as 20 Ma. Because of the presence of a pronounced gravity low in the young Pacific, the origin of which is uncertain, and which is slightly negatively correlated with the residual topography, we chose the threshold as 30 Ma in the Pacific. In the Atlantic, the sediment correction was performed using a linear depth–density relationship. Note that the plate model curves do not follow a \sqrt{t} trend at very young ages, because the initial temperature under the ridge is not constant as a result of melting.

best-fit plate model in the Pacific together with the best-fit models of Parsons & Sclater (1977) and Stein & Stein (1992), who used different data selection criteria to us.

4.1.2 Northwest Atlantic

Results for the Northwest Atlantic are shown in Fig. 7 and listed in Tables A3 and A4. On ocean floor younger than approximately 100 Ma, the half-space cooling model provides a moderately good fit to the subsidence, although the sample size at young ages is rather small. The two sediment corrections discussed above (Section 3.4) are similar on ocean floor younger than 150 Myr, where the sediments are thin in comparison to those at the margin. However, the correction of Loudon *et al.* (2004) is approximately 400 m larger than the correction based on ODP cores for ocean floor older than 150 Myr, perhaps because Crough (1983) underestimated the density of deep compacted sediments, or because the ODP logs are in some way unrepresentative. Therefore, we terminated the reference depth–age table at 150 Ma.

The reference depth–age curves in Fig. 7 again show a departure from \sqrt{t} subsidence that is too rapid to be accounted for using

a conductive plate model. There also appears to be ~ 300 m of shallowing, although the selected topography as a function of age has more scatter than it does in the central Pacific, and the number of blocks within each age bin with small gravity anomalies is small. The age at which the subsidence in Fig. 7(d) departs from a \sqrt{t} trend is slightly greater than in the Pacific, which is consistent with a plate model in which the plate thickness is approximately 100 km. Subtracting the estimated plate cooling gravity field has a larger effect than in the Pacific: Fig. 7(c) shows an unexpected shallowing at approximately 75 Ma, which is not apparent in Fig. 7(d). It is not clear what the reference depth at great age is, although the best-fit plate model predicts that it should be approximately 6.1 km.

4.1.3 Eastern Atlantic

Results for the Northeast and Southeast Atlantic oceans are shown in Fig. 9 and listed in Tables A5–A8. The subsidence as a function of age exhibits less scatter in the Southeast Atlantic than in the Northeast Atlantic, but in both cases a \sqrt{t} trend is apparent at ages younger than 80 Ma. In the Northeast Atlantic, the best-fit thermal plate

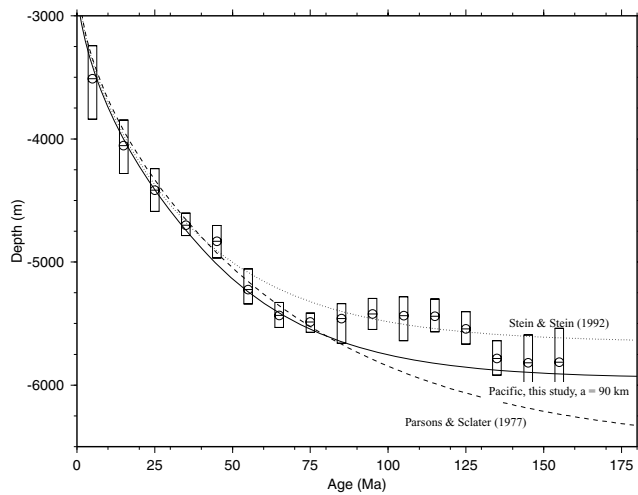


Figure 8. A comparison between our best-fitting Pacific plate model, and the best-fit models of Parsons & Sclater (1977) and Stein & Stein (1992). Parsons & Sclater (1977) used selected data from the deepest parts of the Pacific measured away from seamounts, plateaus and the Hawaiian Swell, and described the subsidence using a model of a 125 km conductive plate, with a basal temperature of 1333°C , a conductivity of $3.1 \text{ W m}^{-1} \text{ K}^{-1}$, and a volume expansivity of $3.28 \times 10^{-5} \text{ K}^{-1}$. As Robinson & Parsons (1988b) acknowledge, the data set Parsons & Sclater (1977) used was biased to deeper values because they did not eliminate measurements taken over regions of negative dynamic topography. Stein & Stein (1992) used sediment-corrected depths from all parts of the Pacific and Atlantic Oceans. By definition, they found the average depth as a function of age to be shallower than that found by Parsons & Sclater (1977), and described the subsidence using a model of a 95-km-thick cooling plate with a basal temperature of 1450°C , a conductivity of $3.1 \text{ W m}^{-1} \text{ K}^{-1}$, and an expansivity of $3.1 \times 10^{-5} \text{ K}^{-1}$. The zero-age depth for all three curves is 2800 m. The data is the same as plotted in Fig. 7(a). Our best-fit plate model provides a poor fit to the variation of depth with age between the ages of 80–130 Ma. Furthermore, because the other authors used different data selection criteria to us, their models do not provide an adequate description of our estimate of the variation of depth with age once they depart from a conductive \sqrt{t} cooling trend either.

thickness is approximately 90 km, given a zero-age depth of 2650 m. A least-squares fit of a \sqrt{t} subsidence curve to the median depths in Fig. 9(b) younger than 80 Ma is $d = -2527 - 336\sqrt{t}$. In the Southeast Atlantic, the best-fit thermal plate thickness is approximately 95 km with a zero-age depth of 2650 m. A least-squares fit of a \sqrt{t} subsidence curve to the median depths in Fig. 9(d) younger than 80 Ma is $d = -2444 - 347\sqrt{t}$. In both regions, the departure from \sqrt{t} subsidence as the ocean ages is more rapid than would be expected given plate-like subsidence, and there is a couple of hundred metres of shallowing at ages in excess of 100 Ma. Because of uncertainty in the sediment correction and the continental margin gravity anomaly, we terminated the reference table at 150 Ma in the Northeast Atlantic and at 120 Ma in the Southeast Atlantic.

4.1.4 North Indian Ocean

Results for the North Indian ocean are shown in Fig. 10(a) and listed in Tables A9 and A10. Because of the limited number of data points and low correlation between topography and gravity at ages in excess of 120 Ma, we terminated the reference table at 120 Ma. There are very few regions with near-zero gravity anomalies, and the depth–age curves calculated using only those regions do not appear to follow a simple \sqrt{t} subsidence trend. However, the entire Indian ocean is covered by a very-long-wavelength

negative gravity anomaly, which has no clear topographic expression. We investigated the effect of subtracting the longest wavelength gravity field before processing the data, and found that it improved the correlation between the selected blocks of gravity and topography significantly (compare Figs 10c and d). The new reference depth–age trend is shown in Fig. 10(b), and is deeper than the trend in Fig. 10a because the baselevel has been shifted; we find the average subsidence is fit well using a model of a 90-km-thick conductive plate. We attempted the same procedure in the Pacific and Northwest Atlantic, but found that it made the correlation worse (for instance, r_s in the Pacific in the age range 90–100 Ma was reduced from 0.89 to -0.22).

4.2 Correlation between gravity and topography over swells and troughs

The correlation between selected 30 min block-medians of gravity and sediment-corrected topography in each age-bin is illustrated in Fig. 11 and described below. For sample sizes larger than 100, the probability that a correlation with $r_s > 0.2$ occurred by chance is less than 5 per cent.

4.2.1 North pacific

The best and most convincing correlations between gravity and topography are in the central Pacific between the ages of 60–110 Ma. The highest correlation coefficient is 0.89 in the age range 90–100 Ma, where the best-fit linear slope is $27.6 \text{ mGal km}^{-1}$ (Table A1). The slope and strong correlation are characteristic of convective swells and troughs (e.g. McKenzie 1994). On older ocean floor, the gravity anomalies are mostly negative. r_s decreases to 0.4–0.6 within individual age bins, and the best-fit slope increases to between 30–40 mGal km^{-1} . This may be a result of unwanted pollution from unexcluded regions of thickened crust (such as small seamounts), which have a higher admittance between topography and gravity than dynamic swells. These results differ little if topography is plotted against residual gravity rather than observed gravity.

4.2.2 Atlantic and Indian

Plots of gravity versus topography show a greater degree of variability in the Atlantic than they do in the Pacific. This may be in part a result of a more pronounced uncompensated surface roughness associated with slower spreading rates (Hayes & Kane 1991) and a lack of variation of dynamic topography within individual age bins. For instance, in the Northwest Atlantic between the ages of 80–90 Ma, the best-fit slope of observed gravity versus topography is 65 mGal km^{-1} (Table A3), which is approximately the expected value for uncompensated crust (e.g. McKenzie & Fairhead 1997, Figure 4a). Elsewhere in the Northwest Atlantic, the slopes vary from 30–40 mGal km^{-1} within individual age bins, with r_s varying from 0.5–0.9. The Northeast Atlantic is more consistent: between the ages of 40–100 Ma the slopes vary from 30–40 mGal km^{-1} , and r_s from 0.5–0.75. Similar results are found in the North Indian ocean once the very-long-wavelength gravity field is removed: between the ages of 40–100 Ma, the slopes within individual age bins vary from 35–45 mGal km^{-1} and the coefficients from 0.5–0.9 (Table A10). In the Southeast Atlantic (Table A7), the slopes are lower (20–25 mGal km^{-1}), as are the correlations (0.2–0.7). Plotting topography versus residual gravity instead of gravity again makes relatively little difference to the results.

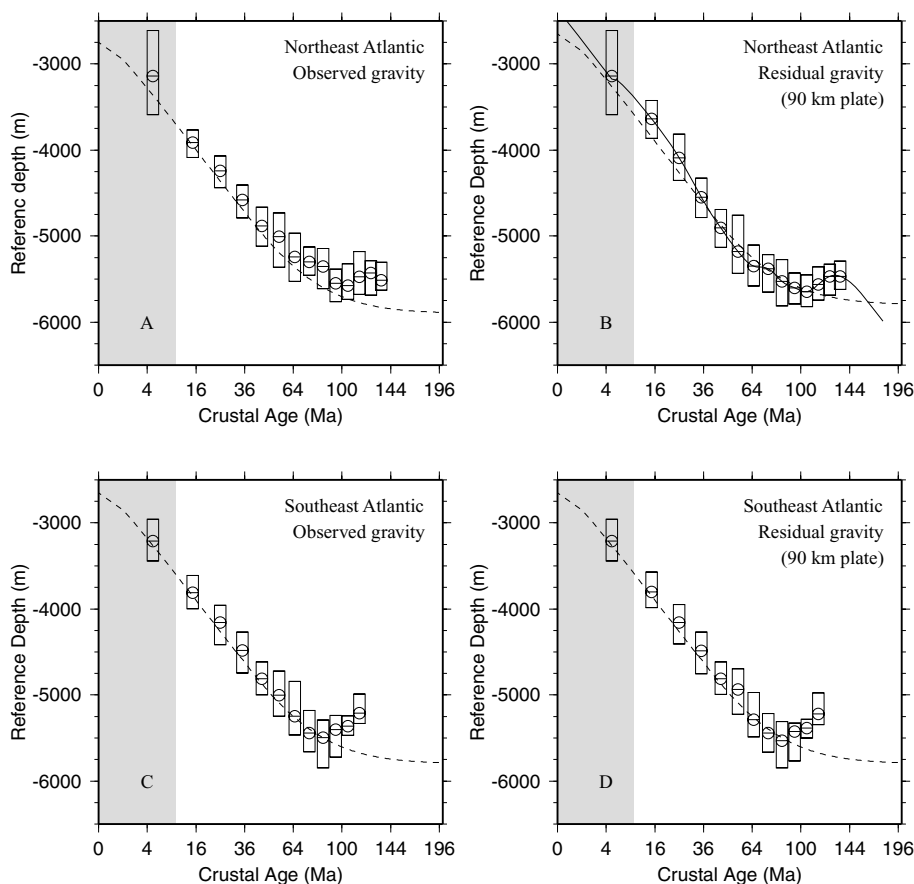


Figure 9. Reference depth versus the square root of age in the Eastern Atlantic.

5 RESIDUAL TOPOGRAPHY AND GRAVITY

Residual topography is defined as the observed topography minus the average topography for crust of that age in the absence of dynamic topography and thickened crust. It is calculated in order to expose broad features in the ocean floor which are not simply a function of the age of the plate. We examined residual depth and gravity in the North Pacific and North Atlantic oceans, where the pattern of swells and troughs is particularly clear.

Fig. 12(a) shows the residual depth in the Pacific (calculated using the solid line in Fig. 7b) after regions of thickened crust have been removed and sediment corrections applied. Fig. 12(b) shows the residual gravity in the same region. Two prominent swells are visible near Hawaii and the Line Islands in both the residual topography and gravity, and are surrounded by smaller depressions. The swells and depressions are aligned in the direction of plate motion with respect to the Hawaiian hotspot and mostly deform crust aged between 60–130 Ma. They are broad features, with characteristic wavelengths longer than 1000 km. We suggest they result from mantle convection, because if they were supported by changes in crustal thickness they would not be associated with gravity anomalies as large as ~ 30 mGal km^{-1} (e.g. McKenzie & Fairhead 1997). Our conclusions agree with those of a recent study by Adam & Bonneville (2005). However, it is difficult to detect the convective signal in the oldest Pacific because a large proportion of the seafloor is covered by thickened crust. In the youngest Pacific, the correlation between residual gravity and topography is small and slightly negative.

Fig. 12(c) shows residual topography after sediment-unloading in the Northeast Atlantic (relative to the solid curve in Fig. 9b). Fig. 12(d) shows residual gravity in the same region. The most prominent features are the Azores and Cape Verde swells and surrounding depressions, which together affect ocean floor of all ages. The Cape Verde swell is aligned approximately parallel to the direction of plate motion with respect to the Iceland hotspot.

Fig. 12(e) shows residual topography after sediment-unloading in the Northwest Atlantic (relative to the solid curve in Fig. 7d). Fig. 12(f) shows residual gravity in the same region. The main feature in the residual topography is the Bermuda Swell and surrounding depressions (Sclater & Wixon 1986), and the residual gravity field shows a similarly shaped anomaly. These features deform crust aged between 75–150 Ma. The swell is elongated perpendicular to the direction of plate motion relative to the Iceland hotspot. Again, we suggest these features result from mantle convection.

To summarize Section 4.2, it appears that the convective scaling between gravity and topography in the North Pacific is approximately 30 mGal km^{-1} . The scaling in the North Atlantic appears to be similar or perhaps slightly larger, but less well constrained. However, in general the relationship between gravity and topography is not wavelength-independent. The best-fit linear slope will be some average of the scaling as a function of wavelength (the admittance) weighted by the power of the coherent parts of the two signals, hence the range of values in Tables A1–A8. Therefore, an alternative is to estimate the admittance $Z(k)$ in the wavenumber domain where the scales can be disentangled. Any variation of admittance with wavelength at long wavelengths provides an important constraint on the convective process (e.g. McKenzie 1977; Parsons & Daly

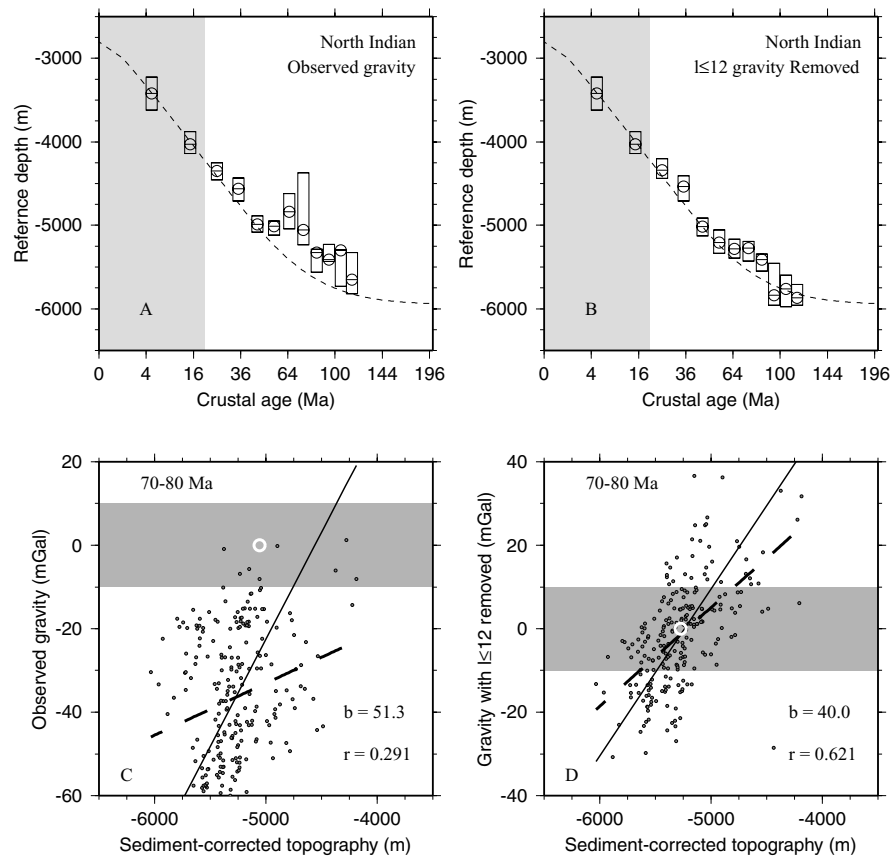


Figure 10. Reference depth versus the square root of age in the North Indian ocean. The full gravity field was used to select the depth values in plot (a). The depth values in plot (b) were selected after the long-wavelength component had been subtracted. The dashed line shows the subsidence of a 90 km plate with a zero-age depth of 2800 m. (c, d). Example gravity–topography scatterplots showing the effect of subtracting the long-wavelength gravity field; the annotations are defined in the caption to Fig. 6. The long-wavelength field was calculated using the GRACE spherical harmonic model GGM02S with the degree-2 coefficients set to zero (Tapley *et al.* 2004). The application of a sharp taper in the spectral domain results in a low-pass filtered gravity field with pronounced and unphysical ripples at a wavenumber corresponding to the cut-off (e.g. Renkin & Sclater 1988). Therefore, a smoothly decreasing taper was chosen: coefficients of degrees 3–8 were unaltered, coefficients of degree 9–12 were multiplied by 0.83, 0.66, 0.33 and 0.17, respectively, and coefficients of degree 13 and higher were set to zero. Degree 12 is equivalent to a wavelength of approximately 3200 km.

1983). Calculations of the admittance in the yellow boxes marked in Fig. 12 are detailed in Appendix C. We find that in the case of swell and trough topography in the North Pacific and North Atlantic, the signals are highly coherent, and the admittance at wavelengths longer than 800 km is not a strong function of wavelength. That is why the linear correlations are so good in the absence of small-scale features such as seamounts. In the Pacific, $Z(k)$ has a value of approximately 25–35 mGal km⁻¹, as expected from Tables A1 and A2. In the Northeast Atlantic over the Cape Verde swell, $Z(k)$ is approximately 20–27 mGal km⁻¹, which is slightly less than expected from Tables A5 and A6. In the Northwest Atlantic over the Bermuda Swell, $Z(k)$ is less well constrained, but appears to be in the range 30–45 mGal km⁻¹, which is in agreement with most of the estimates in Table A3.

6 DISCUSSION

In summary, we obtain two main results. The first is that the departure from half-space subsidence in the absence of dynamic topography, sedimentation, and thickened crust is more rapid than can be accounted for using any conductive plate model; there may even be a small amount of temporary shallowing. The second is that the admittance between gravity and topography over dynamic topogra-

phy in the central Pacific is approximately 30 mGal km⁻¹, varies little with wavelength, is slightly smaller in the Northeast Atlantic, and is slightly larger but less well constrained in the Northwest Atlantic.

The shallowing of the reference depth–age curve for the North Pacific (and to a lesser extent the North Atlantic) between the ages of 80–130 Ma is distinctive, and resembles the results of early numerical experiments of the onset of convection under a cooling lid. In such experiments, the boundary layer is observed to cool by conduction, then to become unstable once its local Rayleigh number exceeds a critical value. The instability continues to grow as it cools, but there is then a sudden increase in the average temperature of the boundary layer as the base of the layer falls off and is replaced by hotter material from below. The new material then cools by conduction, until it in turn becomes unstable, and so on. The result is that the mean temperature structure and hence the subsidence exhibits a series of decaying oscillations about some asymptotic steady-state value. This is consistent with what we observe.

However, we need to ensure that the bulge is not simply an artefact of inadvertently including areas of long-wavelength thickened crust. A useful test is to examine the distribution of depths in some region of the seafloor between 80 and 130 Myr old with a near-zero gravity

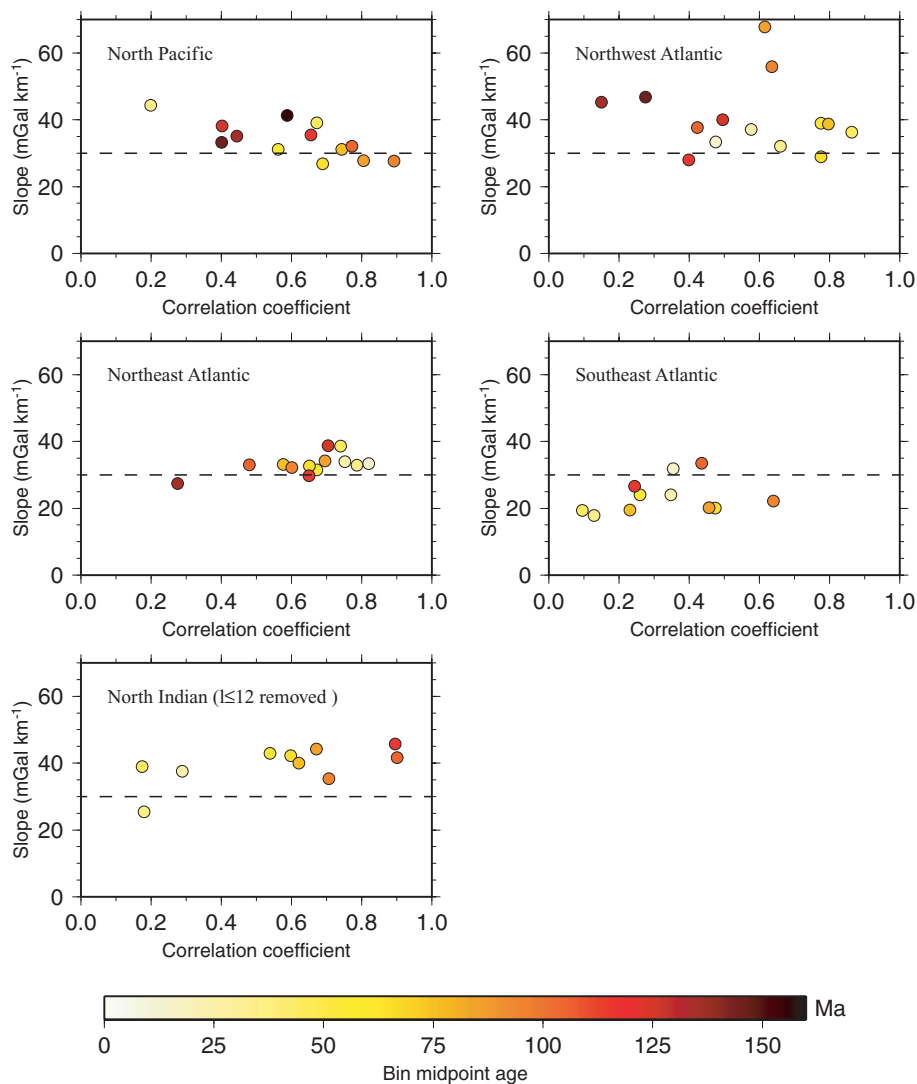


Figure 11. The Spearman's Rank Correlation Coefficient plotted against the best-fit linear slope between selected block-averages of observed sea-surface gravity and topography estimated using the method of Marks & Sandwell (1991). The points are colour-coded by the mid-point crustal age of the bin. The dotted line is a slope of 30 mGal km^{-1} .

anomaly that has clearly not been covered by later lava. One such region is the seafloor south of Hawaii where the original tectonic fabric, including abyssal hills and the Clarion fracture zone, is still expressed in the topography. Depths with gravity anomalies smaller than 5 mGal in a box covering longitudes $195^\circ\text{--}210^\circ$ and latitudes $10^\circ\text{--}20^\circ$ have a mean, median and mode of approximately 5500 m , which is consistent with Fig. 7(b). Finally, there is no evidence that crust created at the ridge in the absence of mantle plumes between 80 and 130 Ma is systematically thicker than crust produced today (White *et al.* 1992).

The reason why Parsons & Sclater (1977) did not find a bulge is because they used seafloor depths where the age was known directly from magnetic anomalies, and by chance the mid-Cretaceous period with no reversals extends throughout much of the region constituting the bulge. A shallowing is visible in the results of later studies (e.g. Renkin & Sclater 1988), but was attributed to plateaus and swells. Here we show that it is in part an intrinsic feature of the ocean lithosphere, and is not predicted by plate cooling models. Nevertheless, the average depth of old ocean floor may still be a good indicator of the thickness of the thermal lithosphere. A useful test

is to compare the predictions of the plate model with observations of heat flow, which is sensitive to the temperature structure in the upper conductive part of the plate. In the Pacific, an average depth of $5.75\text{--}6.0 \text{ km}$ of plate older than 140 Ma implies a plate thickness of approximately 90 km . On Pacific ocean floor older than 100 Ma, the median heat flow is 51 mW m^{-2} , and the inter-quartile range is $43\text{--}59 \text{ mW m}^{-2}$ (Louden 1989; Von Herzen *et al.* 1989; Lister *et al.* 1990). There is no evidence of a systematic variation of heat flow with age once the crustal age exceeds 100 Ma. The predicted heat flow using the model of McKenzie *et al.* (2005) with a 90-km -thick plate at an age of 135 Ma is 48 mW m^{-2} , which is within the range of the observations.

Finally, the scaling between gravity and topography over plume swells provides a constraint on the thickness of the mechanical boundary layer (MBL). The gravity anomaly is the sum of two components: a positive component arising from the elevated topography and a negative component arising from the accumulation of buoyant material under the MBL. The thinner the MBL, the closer the negative mass anomaly is from the observer; therefore, the less its (negative) contribution to the total gravity anomaly is

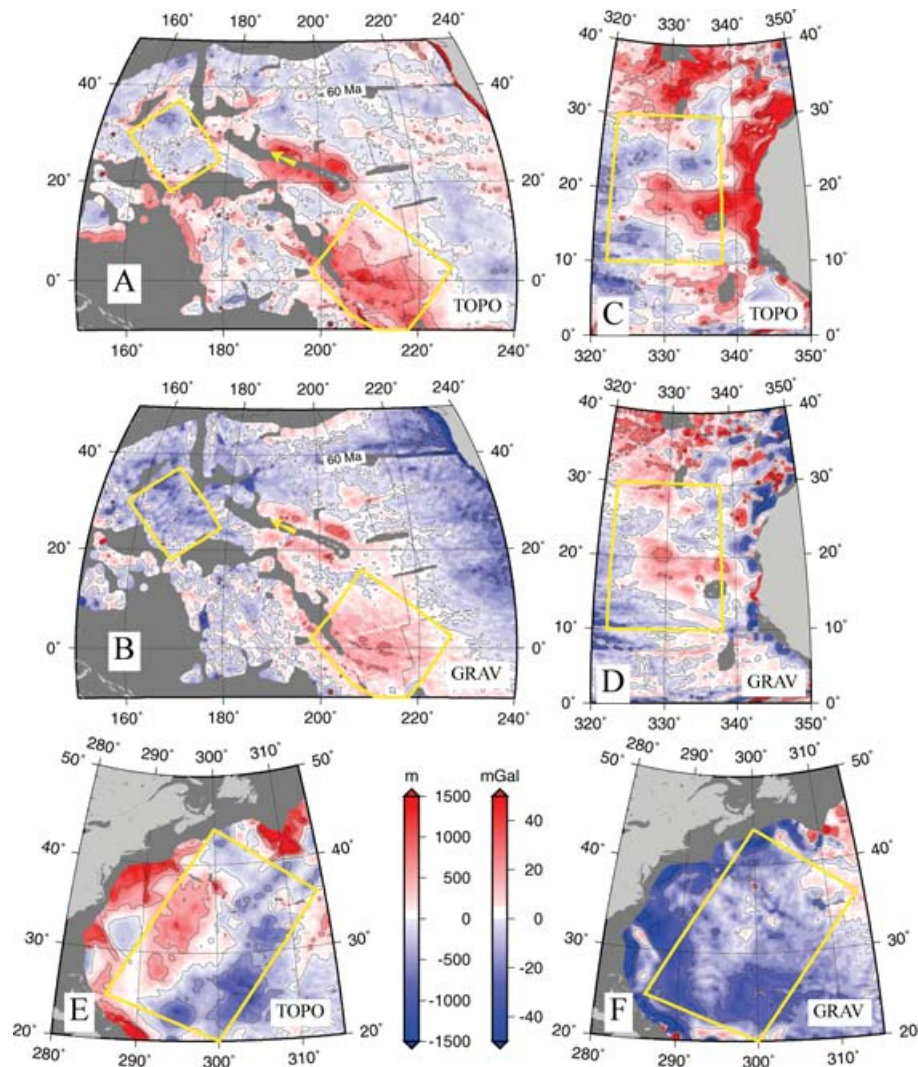


Figure 12. (a) Residual, sediment-corrected and masked topography in the North Pacific calculated with respect to the spline fit of depth versus age (solid curve in Fig. 7b). A Gaussian filter of width 100 km has been applied to smooth the data, which exaggerates the residual topography at the edge of the plateaus which were excluded from the input. The contour interval is 500 m, and the arrow shows the direction of present plate motion relative to the Hawaiian hotspot. The northernmost of the two yellow boxes encloses the region of the Northwest Pacific Basin discussed in Appendix C, and the southern yellow box contains the Line Island swell. The 60 Ma crustal isochron is also marked. Prior to Fourier transforming, the topography and gravity data within each box were projected using an oblique Mercator projection in which both boxes were rectangular. (b) Residual gravity in the North Pacific (90 km plate). The contour interval is 25 mGal. (c) Residual topography in the Northeast Atlantic calculated with respect to the solid curve in Fig. 9(b). The yellow box encloses the Cape Verde Swell. (d) Residual gravity in the Northeast Atlantic (90 km plate). (e) Residual topography in the Northwest Atlantic calculated with respect to the solid curve in Fig. 7(d). The yellow box encloses the Bermuda Swell. (f) Residual gravity in the Northwest Atlantic (100 km plate).

attenuated, and so the lower the overall admittance. McKenzie (1994) performed a number of simple numerical experiments to estimate the admittance over rising plumes, assuming a lid approximately 70 km thick. However, although his mean long-wavelength admittance was approximately 35 mGal km^{-1} , a number of the experiments had unrealistically shallow boxes. For runs with a box thickness close to that of the upper mantle (the maximum was 624 km), the admittance was approximately 30 mGal km^{-1} , which agrees with our results in the central Pacific. Interestingly, our results are also in agreement with the very earliest calculations of the admittance over high Rayleigh number convection in a 2-D box (McKenzie *et al.* 1974). Possible explanations for the slightly higher admittance over the Bermuda Swell are that the buoyant mantle material is further away from the surface than it is in regions such as Hawaii or that the upwelling is no longer active.

7 CONCLUSIONS

When the effects of thickened crust and dynamic topography are excluded, the average variation of depth with age in the North Pacific, the North Indian, the Northwest Atlantic and the Eastern Atlantic oceans is consistent with the conductive cooling and isostatic subsidence of a half-space when the age of the seafloor is less than about 90 Myr. Thereafter, the departure from the half-space cooling curve is more rapid than predicted using simple conductive plate cooling models. The depth–age curves in the Pacific and Atlantic show $\sim 250 \text{ m}$ of temporary shallowing between the ages of 90–130 Myr, which is consistent with the predictions of early numerical convection calculations. However, a 90 km conductive plate provides a reasonable model of the average subsidence of, and heat flux through, old Pacific oceanic lithosphere. In the Pacific, the broad

topographic undulations associated with the Line Island Swell, the Hawaiian Swell, and surrounding basins, have correlated gravity anomalies and an admittance of approximately 30 mGal km^{-1} . They are also aligned in the direction of plate motion with respect to the Hawaiian hotspot, and are likely to result from convective circulation in the upper mantle. A similar situation exists in the Northeast Atlantic, where the dominant features in the residual topography and gravity are the Azores and Cape Verde Swells and surrounding depressions. In the Northwest Atlantic, over the Bermuda Swell, the admittance is slightly larger but also less well constrained.

ACKNOWLEDGMENTS

We thank James Jackson for his help, and the Royal Society and Scripps Institution of Oceanography for support. Comments from Seth Stein and an anonymous reviewer helped us make a number of improvements to the manuscript.

REFERENCES

- Abrams, L.J., Larson, R.L., Shipley, T.H. & Lancelot, Y., 1993. Cretaceous volcanic sequences and Jurassic ocean crust in the East Mariana Basin of the Western Pacific, in *The Mesozoic Pacific: Geology, Tectonics and Volcanism, Geophysical Monograph 77*, pp. 77–101, American Geophysical Union.
- Adam, C. & Bonneville, A., 2005. Extent of the South Pacific Superswell, *J. geophys. Res.*, **110**, B09408, doi:10.1029/2004JB003465.
- Anderson, R.N., McKenzie, D. & Sclater, J.G., 1973. Gravity, bathymetry and convection in the Earth, *Earth planet. Sci. Lett.*, **18**, 391–407.
- Carlson, R.L. & Johnson, H.P., 1994. On modelling the thermal evolution of the oceanic upper mantle: An assessment of the cooling plate model, *J. geophys. Res.*, **99**, 3201–3214.
- Cochran, J.R. & Talwani, M., 1977. Free-air gravity anomalies in the world's oceans and their relationship to residual elevation, *Geophys. J. R. astr. Soc.*, **50**, 495–552.
- Coffin, M.G. & Eldholm, O., 1994. Large igneous provinces: crustal structure, dimensions, and external consequences, *Rev. Geophys.*, **32**, 1–36.
- Colin, P. & Fleitout, L., 1990. Topography of the ocean floor: thermal evolution of the lithosphere and interaction of deep mantle heterogeneities with the lithosphere, *Geophys. Res. Lett.*, **17**(11), 1961–1964.
- Crough, T.S., 1983. The correction for sediment loading on the seafloor, *J. geophys. Res.*, **88**, 6449–6454.
- Davis, E.E. & Lister, C.R.B., 1974. Fundamentals of ridge crest topography, *Earth planet. Sci. Lett.*, **21**, 405–413.
- DeLaughter, J., Stein, S. & Stein, C.A., 1999. Extraction of a lithospheric cooling signal from oceanwide geoid data, *Earth planet. Sci. Lett.*, **174**, 173–181.
- Divins, D., 2004. Total sediment thickness of the world's oceans and marginal seas, online dataset, <http://www.ngdc.noaa.gov/mgg/sedthick/sedthick.html>.
- Doin, M.P. & Fleitout, L., 2000. Flattening of the oceanic topography and geoid: thermal versus dynamic origin, *Geophys. J. Int.*, **143**, 582–594.
- Farrar, E. & Dixon, J.M., 1981. Early Tertiary rupture of the Pacific plate: 1700 km of dextral offset along the Emperor Trough-Line Islands lineament, *Earth planet. Sci. Lett.*, **53**, 307–332.
- Hayes, D.E., 1988. Age-depth relationships and depth anomalies in the Southeast Indian Ocean and South Atlantic Ocean, *J. geophys. Res.*, **93**, 2937–2954.
- Hayes, D.E. & Kane, K.A., 1991. The Dependence of Seafloor Roughness on Spreading Rate, *Geophys. Res. Lett.*, **18**, 1425–1428.
- Heestand, R.L. & Crough, S.T., 1981. The Effect of Hot Spots on the Oceanic Age-Depth Relation, *J. geophys. Res.*, **86**, 6107–6114.
- Hillier, J.K. & Watts, A.B., 2005. The relationship between depth and age in the North Pacific ocean, *J. geophys. Res.*, **110**, B02405, doi:10.1029/2004JB003406.
- Houseman, G. & McKenzie, D.P., 1982. Numerical experiments on the onset of convective instability in the Earth's mantle, *Geophys. J. R. astr. Soc.*, **68**, 133–164.
- Huang, J. & Zhong, S., 2005. Sublithospheric small-scale convection and its implications for the residual topography at old ocean basins and the plate model, *J. geophys. Res.*, **110**, B05404, doi:10.1029/2004JB003153.
- Kido, M. & Seno, T., 1994. Dynamic topography compared with residual depth anomalies in oceans and implications for age-depth curves, *Geophys. Res. Lett.*, **21**, 717–720.
- Marty, J.C. & Cazenave, A., 1989. Regional variations in subsidence rate of oceanic plates: a global analysis, *Earth planet. Sci. Lett.*, **94**, 301–315.
- Lambeck, K., 1972. Gravity anomalies over ocean ridges, *Geophys. J. R. astr. Soc.*, **30**, 37–53.
- LDEO online catalogue of ODP and DSDP logging results. <http://www.ldeo.columbia.edu/BRG/ODP/DATABASE/DATA/search.html>
- Levitt, D.A. & Sandwell, D.T., 1995. Lithospheric bending at subduction zones based on depth soundings and satellite gravity, *J. geophys. Res.*, **100**, 379–400.
- Lister, C.R.B., Sclater, J.G., Davis, E.E., Villinger, H. & Nagihara, S., 1990. Heat flow maintained in ocean basins of great age: investigations in the north equatorial west Pacific, *Geophys. J. Int.*, **102**, 603–630.
- Louden, K.E., 1989. *CRC Handbook of Seafloor Heat Flow*, CRC Press, Boca Raton, Florida.
- Louden, K.E., Tucholke, B.E. & Oakley, G.N., 2004. Regional anomalies of sediment thickness, basement depth and isostatic crustal thickness in the north Atlantic ocean, *Earth planet. Sci. Lett.*, **224**, 193–211.
- Mammerickx, J. & Sharman, G.F., 1988. Tectonic evolution of the North Pacific during the Cretaceous quiet period, *J. geophys. Res.*, **93**, 3009–3024.
- Marks, K.M. & Sandwell, D.T., 1991. Analysis of geoid height versus topography for oceanic plateaus and swells using nonbiased linear regression, *J. geophys. Res.*, **96**, 8045–8055.
- McKenzie, D., 1977. Surface deformation, gravity anomalies and convection, *Geophys. J. R. astr. Soc.*, **48**, 211–238.
- McKenzie, D., 1994. The relationship between topography and gravity on Earth and Venus, *Icarus*, **112**, 55–88.
- McKenzie, D. & Bickle, M.J., 1988. The volume and composition of melt generated by extension of the lithosphere, *J. Petrol.*, **29**, 625–679.
- McKenzie, D. & Fairhead, D., 1997. Estimates of the effective elastic thickness of the continental lithosphere from Bouguer and free-air gravity anomalies, *J. geophys. Res.*, **102**, 27 523–27 552.
- McKenzie, D. & Nimmo, F., 1997. Elastic thickness estimates for Venus from line of sight accelerations, *Icarus*, **130**, 198–216.
- McKenzie, D., Roberts, J.M. & Weiss, N.O., 1974. Convection in the Earth's Mantle: towards a numerical solution, *J. Fluid. Mech.*, **62**, 465–538.
- McKenzie, D., Jackson, J. & Priestley, K., 2005. Thermal structure of oceanic and continental lithosphere, *Earth planet. Sci. Lett.*, **233**, 337–349.
- McNutt, M., 1979. Compensation of oceanic topography: An application of the response function technique to the Surveyor area, *J. geophys. Res.*, **84**, 7589–7598.
- Müller, R.D., Roest, W.R., Royer, J.-Y., Gahagan, L.M. & Sclater, J.G., 1997. Digital isochrons of the world's ocean floor, *J. geophys. Res.*, **102**, 3211–3214.
- Parsons, B. & Daly, S., 1983. The relationship between surface topography, gravity anomalies, and temperature structure of convection, *J. geophys. Res.*, **88**, 1129–1144.
- Parsons, B. & McKenzie, D., 1978. Mantle convection and the thermal structure of the plates, *J. geophys. Res.*, **83**, 4485–4496.
- Parsons, B. & Sclater, J.G., 1977. An analysis of the variation of ocean floor bathymetry and heat flow with age, *J. geophys. Res.*, **82**, 803–827.
- Pérez-Gussinyé, M., Lowry, A.R., Watts, A.B. & Velicogna, I., 2004. On the recovery of effective elastic thickness using spectral methods: examples from synthetic data and from the Fennoscandian Shield, *J. geophys. Res.*, **109**, B10409, doi:10.1029/2003JB002788.
- Phipps Morgan, J. & Smith, W.H.F., 1992. Flattening of the sea floor depth-age curve as a response to asthenospheric flow, *Nature*, **359**, 524–527.

- Press, W.H., Teukolsky, S.A., Vetterling, W.T. & Flannery, B.P., 1992. *Numerical Recipes in C: The Art of Scientific Computing*, Cambridge University Press, Cambridge.
- Rea, D.K. & Dixon, J.M., 1983. Late Cretaceous and Paleogene tectonic evolution of the North Pacific Ocean, *Earth planet. Sci. Lett.*, **65**, 145–166.
- Renkin, M.L. & Sclater, J.G., 1988. Depth and age in the North Pacific, *J. geophys. Res.*, **93**, 2919–2935.
- Richter, F.M. & McKenzie, D.P., 1981. Parameterizations for the horizontally-averaged temperature of infinite Prandtl Number convection, *J. geophys. Res.*, **86**, 1738–1744.
- Robinson, E.M. & Parsons, B., 1988a. Effect of a shallow, low viscosity zone on small-scale instabilities under the cooling oceanic plates, *J. geophys. Res.*, **93**, 3468–3479.
- Robinson, E.M. & Parsons, B., 1988b. Effect of a shallow, low viscosity zone on the formation of mid-plate swells, *J. geophys. Res.*, **93**, 3144–3156.
- Sandwell, D.T. & Renkin, M.L., 1988. Compensation of swells and plateaus in the North Pacific: no direct evidence for mantle convection, *J. geophys. Res.*, **93**, 2775–2783.
- Sandwell, D.T. & Smith, W.H.F., 1997. Marine gravity anomaly from Geosat and ERS 1 satellite altimetry, *J. geophys. Res.*, **102**, 10 039–10 054.
- Schroeder, W., 1984. The empirical age-depth relation and depth anomalies in the Pacific ocean basin, *J. geophys. Res.*, **89**, 9873–9883.
- Sclater, J.G. & Wixon, L., 1986. The relationship between depth and age and heat flow and age in the western North Atlantic, in *The Geology of North America, volume M, the western North Atlantic region*, pp. 257–270, Geological Society of America.
- Sclater, J.G., Anderson, R.N. & Bell, M.L., 1971. Elevation of ridges and evolution of the central eastern Pacific, *J. geophys. Res.*, **76**, 7888–7915.
- Sclater, J.G., Lawver, L.A. & Parsons, B., 1975. Comparison of long-wavelength residual elevation and free-air gravity anomalies in the North Atlantic and possible implications for the thickness of the lithospheric plate, *J. geophys. Res.*, **80**, 1031–1052.
- Shoberg, T., Stein, C. & Stein, S., 1993. Constraints on lithospheric thermal structure for the Indian ocean basin from depth and heat flow data, *Geophys. Res. Lett.*, **20**, 1095–1098.
- Smith, W.H.F. & Sandwell, D.T., 1997. Global sea floor topography from satellite altimetry and ship depth soundings, *Science*, **277**, 1956–1962.
- Smith, W.H.F. & Wessel, P., 1990. Gridding with continuous curvature splines in tension, *Geophysics*, **55**, 293–305.
- Stein, C.A. & Stein, S., 1992. A model for the global variation in oceanic depth and heat flow with age, *Nature*, **359**, 123–129.
- Tapley, B.D., Bettadpur, S., Watkins, M.M. & Reigber, C.H., 2004. The Gravity Recovery and Climate Experiment: mission overview and early results, *Geophys. Res. Lett.*, **31**, L09607, doi:10.1029/2004GL019920.
- Tucholke, B.E., Houtz, R.E. & Ludwig, W.J., 1982. Sediment thickness and depth to basement in western North Atlantic basin, *Bull. Am. Assoc. Pet. Geol.*, **66**, 1384–1395.
- Turcotte, D. & Schubert, G., 2002. *Geodynamics*, 2nd edn, Cambridge University Press, Cambridge.
- Von Herzen, R.P., Condrey, M.J., Detrick, R.S. & Fang, C., 1989. Heat flow and the thermal origin of hot spot swells: the Hawaiian swell revisited, *J. geophys. Res.*, **94**, 13 783–13 799.
- Watts, A.B., 1976. Gravity and bathymetry in the central Pacific ocean, *J. geophys. Res.*, **81**, 1533–1553.
- Watts, A.B., McKenzie, D.P., Parsons, B.E. & Rofoussé, M., 1985. The relationship between gravity in the Pacific ocean, *Geophys. J. R. astr. Soc.*, **83**, 263–298.
- Wessel, P. & Smith, W.H.F., 1998. New, improved version of Generic Mapping Tools released, *EOS, Trans. Am. geophys. Un.*, **79**, 579.
- White, R.S., McKenzie, D. & O’Nions, R.K., 1992. Oceanic crustal thickness from seismic measurements and Rare Earth Element inversions, *J. geophys. Res.*, **97**, 19 683–19 715.
- Wolfe, C.J. & McNutt, M.K., 1991. Compensation of Cretaceous seamounts of the Darwin Rise, Northwest Pacific Ocean, *J. geophys. Res.*, **96**, 2363–2374.

APPENDIX A: RESULTS TABLES

Tables A1–A10 present full analysis of depth as a function of age.

Table A1. Full analysis of unperturbed depth as a function of age for the North Pacific. NB denotes the number of 30 min blocks that remain after all the masks have been applied, NBU is the number that were used to calculate the three quartiles of the depth in columns 6–8. All depths are in metres. For ages older than 30 Ma, only those blocks with gravity anomalies smaller than 5 mGal were used to calculate the depth quartiles. r_s is the Spearman’s Rank Correlation Coefficient between gravity and topography, b is the best-fitting linear slope (in mGal km⁻¹) using the method of Marks & Sandwell (1991) when topography is plotted against gravity. Between 160–180 Ma, the correlation is almost zero, and we are concerned about possible pollution from thickened crust and flexural effects. Therefore, we judge this data to be unreliable.

Age bin (Ma)	NB	NBU	r_s	b	LQ	Median	UQ
0–10	1985	1985	–	–	3243	3512	3839
10–20	989	160	–0.339	–	4072	4289	4373
20–30	1443	274	–0.358	–	4417	4582	4728
30–40	1195	277	0.198	37.5	4604	4701	4785
40–50	1307	505	0.672	39.1	4703	4831	4968
50–60	884	400	0.562	31.1	5056	5224	5341
60–70	651	296	0.689	26.8	5329	5433	5532
70–80	766	379	0.743	31.2	5414	5488	5572
80–90	712	305	0.806	27.8	5337	5460	5661
90–100	590	121	0.892	27.6	5296	5423	5549
100–110	580	152	0.772	32.1	5281	5437	5640
110–120	1394	499	0.655	35.5	5300	5441	5566
120–130	863	270	0.402	38.2	5404	5543	5668
130–140	896	123	0.444	35.1	5640	5784	5918
140–150	538	112	0.401	33.3	5592	5818	6051
150–160	448	95	0.588	41.3	5539	5814	5980
160–180	442	166	0.010	31.0	5537	5844	6067

Table A2. Full analysis of depth as a function of age for the North Pacific, using residual gravity rather than observed gravity.

Age bin (Ma)	NB	NBU	r_s	b	LQ	Median	UQ
10–20	989	142	–0.398	–	4106	4295	4376
20–30	1443	243	–0.390	–	4445	4602	4731
30–40	1195	281	0.181	36.3	4617	4703	4782
40–50	1307	481	0.678	36.5	4733	4868	4975
50–60	884	428	0.572	28.9	5064	5232	5335
60–70	651	319	0.725	26.5	5381	5481	5559
70–80	766	352	0.757	31.1	5446	5509	5601
80–90	712	296	0.804	27.7	5399	5539	5717
90–100	590	151	0.885	27.1	5410	5579	5718
100–110	580	169	0.779	31.8	5390	5598	5706
110–120	1394	473	0.658	35.6	5333	5472	5610
120–130	863	324	0.403	38.1	5437	5574	5699
130–140	896	171	0.447	35.1	5668	5811	5958
140–150	538	145	0.401	33.4	5594	5850	6099
150–160	448	118	0.586	41.3	5703	5886	6030
160–180	442	183	0.014	30.9	5578	5844	6092

Table A3. Full analysis of depth as a function of age for the Northwest Atlantic, using observed gravity rather than residual gravity, and the linear depth–density relationship to make the sediment correction.

Age bin (Ma)	NB	NBU	r_s	b	LQ	Median	UQ
0–10	56	56	–	–	3201	3332	3663
10–20	64	49	0.476	33.4	3811	3992	4085
20–30	69	47	0.577	37.1	4230	4360	4513
30–40	90	41	0.660	32.1	4401	4667	4869
40–50	105	44	0.863	36.3	4751	4902	5014
50–60	102	25	0.776	39.0	5050	5102	5170
60–70	98	11	0.775	28.9	4943	5046	5152
70–80	126	22	0.797	38.7	5158	5299	5556
80–90	162	27	0.616	67.8	5638	5768	5805
90–100	165	36	0.635	55.9	5675	5800	5839
100–110	194	77	0.423	37.7	5263	5746	5851
110–120	235	78	0.399	28.0	5084	5480	5824
120–130	150	32	0.496	40.0	5085	5319	5631
130–140	125	6	0.150	45.3	5652	5652	6232
140–150	163	8	0.276	46.8	5335	5612	5658

Table A4. Full analysis of depth as a function of age for the Northwest Atlantic, using residual gravity rather than observed gravity, and the linear depth–density relationship to make the sediment correction.

Age bin (Ma)	NB	NBU	r_s	b	LQ	Median	UQ
10–20	64	31	0.326	32.6	3785	3941	4072
20–30	69	32	0.557	36.0	4165	4352	4445
30–40	90	30	0.630	31.3	4353	4561	4748
40–50	105	37	0.857	36.2	4744	4893	4983
50–60	102	27	0.778	40.9	5042	5102	5198
60–70	98	16	0.764	31.0	5128	5238	5522
70–80	126	23	0.798	40.4	5275	5384	5654
80–90	162	27	0.614	74.5	5750	5784	5930
90–100	165	45	0.628	59.3	5760	5820	5889
100–110	194	80	0.405	39.8	5249	5767	5869
110–120	235	110	0.364	29.4	5169	5460	5842
120–130	150	63	0.466	38.2	5238	5463	5929
130–140	125	22	0.096	46.4	5649	6046	6223
140–150	163	33	0.250	47.3	5612	5671	6165

Table A5. Full analysis of depth as a function of age for the Northeast Atlantic, using observed gravity rather than residual gravity, and the linear depth–density relationship to make the sediment correction.

Age bin (Ma)	NB	NBU	r_s	b	LQ	Median	UQ
0–10	171	171	–	–	2613	3139	3587
10–20	200	43	0.820	33.4	3765	3915	4087
20–30	224	83	0.752	33.9	4068	4242	4437
30–40	256	108	0.787	32.9	4408	4581	4791
40–50	268	140	0.740	38.6	4665	4881	5117
50–60	258	123	0.672	31.5	4730	5006	5361
60–70	228	111	0.651	32.7	4965	5244	5525
70–80	254	152	0.577	33.1	5127	5302	5457
80–90	277	171	0.696	34.2	5143	5355	5611
90–100	303	194	0.601	32.2	5383	5550	5762
100–110	311	184	0.480	33.0	5320	5574	5734
110–120	229	132	0.650	29.7	5181	5474	5679
120–130	123	68	0.705	38.7	5286	5430	5685
130–140	98	57	0.275	27.4	5304	5515	5627

Table A6. Full analysis of depth as a function of age for the Northeast Atlantic, using residual gravity rather than observed gravity, and the linear depth–density relationship to make the sediment correction.

Age bin (Ma)	NB	NBU	r_s	b	LQ	Median	UQ
10–20	200	106	0.756	35.2	3433	3639	3866
20–30	224	110	0.669	36.4	3814	4089	4355
30–40	256	107	0.708	33.7	4327	4551	4786
40–50	268	146	0.706	39.9	4690	4904	5132
50–60	258	139	0.640	30.2	4758	5180	5433
60–70	228	116	0.650	31.4	5105	5349	5581
70–80	254	149	0.577	33.2	5216	5380	5649
80–90	277	154	0.696	32.9	5274	5527	5811
90–100	303	185	0.607	31.5	5431	5602	5788
100–110	311	184	0.440	34.7	5453	5648	5819
110–120	229	130	0.639	30.0	5357	5561	5744
120–130	123	71	0.704	39.6	5328	5468	5686
130–140	98	69	0.255	27.0	5292	5468	5619

Table A7. Full analysis of depth as a function of age for the Southeast Atlantic, using observed gravity rather than residual gravity, and the linear depth–density relationship to make the sediment correction.

Age bin (Ma)	NB	NBU	r_s	b	LQ	Median	UQ
0–10	477	477	–	–	2957	3210	3440
10–20	459	314	0.354	31.9	3613	3812	3997
20–30	524	414	0.348	24.0	3956	4158	4414
30–40	357	291	0.129	17.9	4271	4482	4743
40–50	185	159	0.096	19.4	4615	4810	5000
50–60	161	125	0.260	24.0	4722	5001	5247
60–70	148	120	0.475	20.1	4840	5247	5465
70–80	209	143	0.231	19.5	5178	5440	5658
80–90	205	173	0.457	20.2	5292	5496	5846
90–100	239	187	0.640	22.2	5240	5401	5722
100–110	318	231	0.435	33.5	5244	5362	5468
110–120	367	277	0.244	26.6	4987	5209	5331

Table A8. Full analysis of depth as a function of age for the Southeast Atlantic, using residual gravity rather than observed gravity, and the linear depth–density relationship to make the sediment correction.

Age bin (Ma)	NB	NBU	r_s	b	LQ	Median	UQ
10–20	459	333	0.325	34.1	3571	3804	3984
20–30	524	411	0.399	23.8	3949	4156	4406
30–40	357	288	0.196	17.5	4271	4487	4754
40–50	185	165	0.130	18.9	4615	4809	4994
50–60	161	128	0.295	23.0	4696	4937	5226
60–70	148	110	0.483	21.0	4969	5285	5487
70–80	209	144	0.209	20.0	5214	5440	5666
80–90	205	169	0.528	19.8	5310	5533	5847
90–100	238	191	0.680	22.5	5326	5426	5767
100–110	318	229	0.437	34.2	5282	5385	5501
110–120	367	268	0.196	27.5	4975	5128	5344

Table A9. Full analysis of depth as a function of age for the North Indian Ocean, using observed gravity rather than residual gravity.

Age (Ma)	NB	NBU	r_s	b	LQ	Median	UQ
0–10	161	161	–	–	3226	3419	3620
10–20	145	145	–	–	3876	4030	4130
20–30	126	111	0.275	69.0	4249	4347	4454
30–40	128	104	0.101	64.2	4434	4560	4710
40–50	177	86	0.364	39.1	4888	4991	5084
50–60	407	50	0.567	45.0	4951	5010	5118
60–70	376	26	0.605	51.4	4621	4837	5044
70–80	230	8	0.291	51.3	4372	5057	5235
80–90	120	6	0.057	45.7	5287	5327	5561
90–100	92	6	0.613	34.8	5228	5412	5432
100–110	125	5	0.740	24.4	5297	5301	5730
110–120	86	4	0.319	29.8	5326	5653	5818

Table A10. Full analysis of depth as a function of age for the North Indian Ocean, but with the long wavelength ($l \leq 12$) gravity field subtracted prior to plotting gravity versus topography.

Age (Ma)	NB	NBU	r_s	b	LQ	Median	UQ
20–30	126	104	0.289	37.6	4202	4340	4432
30–40	128	113	0.180	25.4	4406	4535	4709
40–50	177	143	0.174	39.0	4913	5016	5125
50–60	407	299	0.539	42.9	5057	5207	5336
60–70	376	269	0.598	42.2	5165	5284	5394
70–80	230	139	0.621	40.0	5192	5273	5431
80–90	120	59	0.671	44.2	5345	5413	5548
90–100	92	44	0.707	35.3	5454	5837	5959
100–110	125	49	0.901	41.6	5599	5762	5976
110–120	86	47	0.895	45.7	5710	5867	5958

APPENDIX B: ESTIMATING THE PLATE COOLING CONTRIBUTION TO THE GRAVITY FIELD

Providing topography is compensated isostatically, and the associated lithospheric density anomalies ($\Delta\rho$) vary much more rapidly in the vertical direction (z) than they do in the horizontal direction

(x, y), Turcotte & Schubert (2002) show that the anomaly in gravitational potential over the topography is approximately proportional to the first moment of the vertical density distribution.

$$\Delta U(x, y) = -2\pi G \int_0^h z \Delta\rho(x, y, z) dz, \quad (\text{B1})$$

where h is the depth to which density anomalies persist. The potential anomaly over a cooling plate, which has subsided by an amount w , and where $\Delta\rho$ is the density contrast between the lithosphere and the ridge, is, to first order:

$$\Delta U(x, y) = -2\pi G \left\{ \frac{(\rho_0 - \rho_w)w^2}{2} + \int_0^a z \Delta\rho(x, y, z) dz \right\}, \quad (\text{B2})$$

where a is the thermal plate thickness, $z = 0$ is at the sea floor ρ_0 is the density of cold mantle, and ρ_w is the density of water.

We first low-pass filtered the crustal age model by continuing it over the globe (Smith & Wessel 1990; Wessel & Smith 1998) and expanded it in spherical harmonics to degree and order 90. We excluded the Pacific marginal basins first in order to reduce ringing at sharp boundaries. A grid of anomalous potential relative to the ridge was then calculated using the low-pass filtered age grid and eq. (B2). We used the temperature field from the numerical plate model of McKenzie *et al.* (2005), and their expression for density as a function of temperature. We then expanded the grid of anomalous potential in spherical harmonics to degree and order 120, and calculated the radial component of the surface gravity field Δg using eq. (B3) (e.g. McKenzie & Nimmo 1997).

$$\Delta g = -\frac{GM}{R^2} \sum_{l=0}^{120} (l+1) \sum_{m=0}^l [C_{lm} \cos(m\lambda) + S_{lm} \sin(m\lambda)] \bar{P}_{lm}(\cos\theta), \quad (\text{B3})$$

where C_{lm} and S_{lm} are Spherical Harmonic coefficients of degree l and order m of the anomalous potential. λ is longitude and θ co-latitude. \bar{P}_{lm} is the normalized Legendre polynomial and R the Earth's radius. M is the mass of the Earth and G the universal gravitational constant.

Fig. B1 illustrates the predicted plate cooling contribution to the global gravity field from a 90 km plate. Away from the ridge, the plate cooling contribution is small. There is, of course, a contradiction in

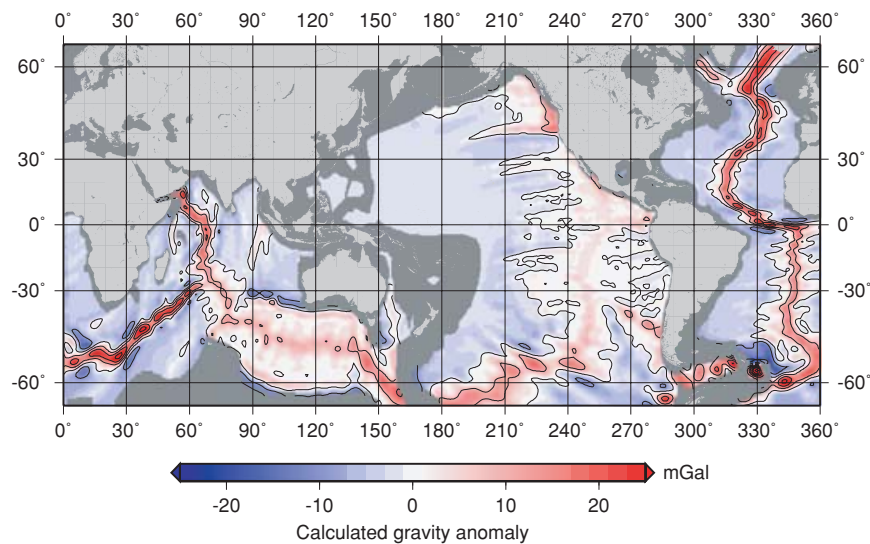


Figure B1. Estimated plate cooling contribution to the gravity field assuming a 90 km conductive plate model. The contour level is 10 mGal. The largest anomalies are found near slow-spreading ridges, such as in the central Atlantic and the Southwest Indian Ocean. In the old oceans, the anomalies are negative but small (<5 mGal).

our approach in that we use the plate model to calculate the residual gravity field, but at the same time argue that the plate model is not a good description of the thermal state of the lithosphere after the onset of instability. However, the plate gravity anomaly is largely confined to the vicinity of the ridge where the plate model is applicable; furthermore, there is also no alternative given our uncertainty about the nature of convective instabilities under the plates.

APPENDIX C: ADMITTANCE ANALYSIS OF SWELLS AND TROUGHS IN THE NORTH PACIFIC AND NORTH ATLANTIC

In the absence of noise, the isotropic admittance $Z(k)$ relates the Fourier transform of the gravity $g(k_x, k_y)$ to the Fourier transform

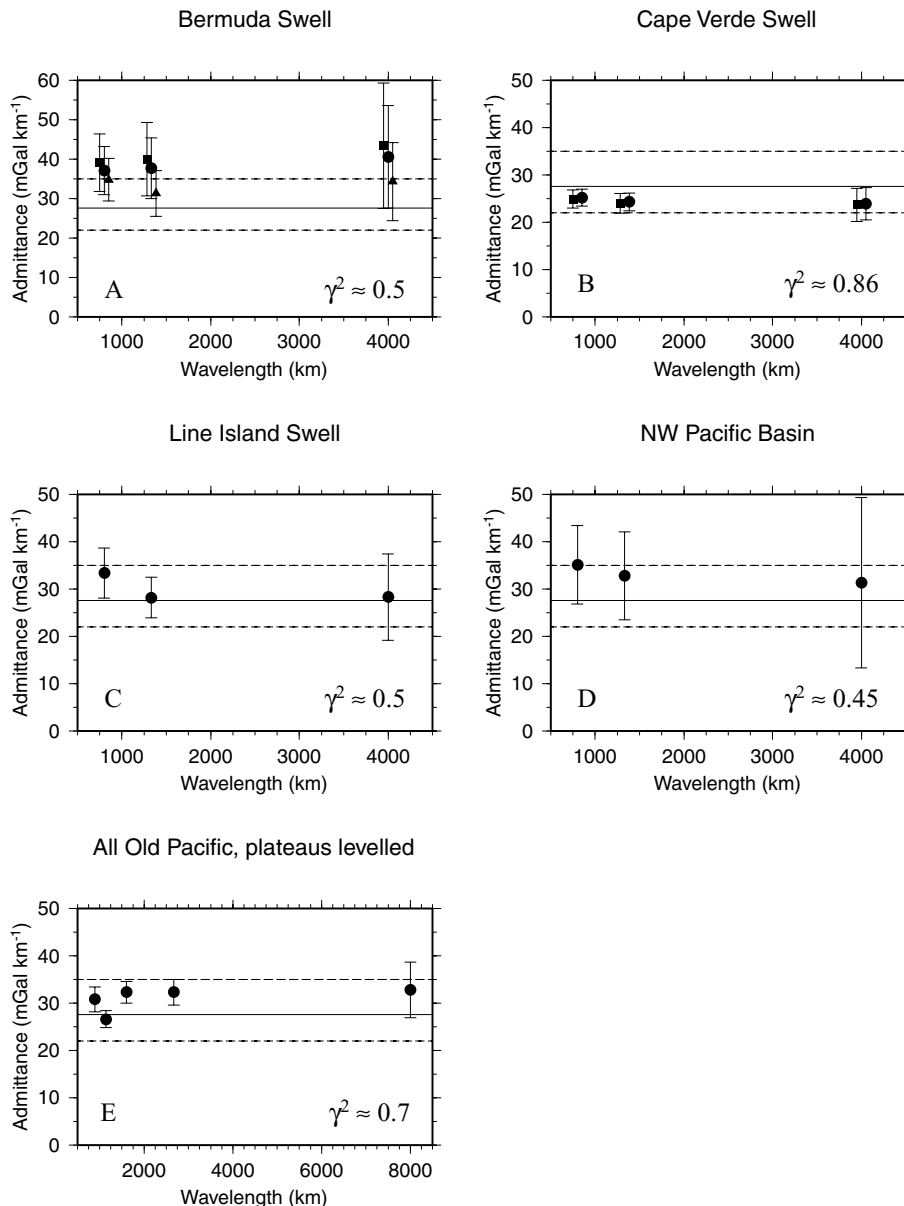


Figure C1. (a–d) Intermediate- to long-wavelength admittance over the yellow boxes marked on Fig. 12. The approximate coherence (γ^2) is also indicated, which in no case varies strongly with wavelength. The estimates of Z_3 are averages over three wavenumber annuli in 2-D wavenumber space centred on radial wavelengths of 800, 1330 and 4000 km. The exact choice of centre wavenumbers is unimportant: similar results are found if averaging is done over a slightly different number of annuli with different central wavenumbers. Plot (a) **circles**: admittance between observed gravity and the residual topography calculated using the solid curve in Fig. 7(d); **squares**: residual gravity (assuming a 100 km plate) and residual topography calculated using the solid curve in Fig. 7(d); **triangles**: residual gravity and the residual topography using the solid curve in Fig. 7(b) (the Pacific), for comparison and in order to assess the sensitivity of Z_3 to the depth–age curve used to calculate the residual topography. In plot (b) the residual gravity was calculated assuming a 90 km plate and the residual topography with respect to the solid curve in Fig. 9(b). Plots (c) and (d) were calculated using residual gravity (assuming a 90 km plate) and residual topography with respect to the solid curves in Figs 7(b) and (d). Plot (e) is an estimate of Z_3 within the large Pacific box illustrated in Fig. C2 with large regions of thickened crust levelled, for five wavenumber annuli centred on radial wavelengths of 900, 1140, 1600, 2700 and 8000 km. The solid line marked on all plots is our best estimate of the convective gravity–topography scaling in the central Pacific (27.6 mGal km⁻¹). The upper dotted line marked on all plots is the value of 35 mGal km⁻¹ estimated by McKenzie (1994), the lower dotted line marked on all plots an early estimate of 22 mGal km⁻¹ in the central Pacific by Watts (1976). If there is noise in the gravity, $1/Z_3$ will be an overestimate of the true admittance.

of the topography $t(k_x, k_y)$:

$$g = Zt, \quad (\text{C1})$$

where k_x and k_y are the wavenumbers in the x and y directions, respectively, and the true wavenumber $k = \sqrt{k_x^2 + k_y^2}$. If there is noise $n(k_x, k_y)$ in the gravity [i.e. $g = Z_1t + n$], then the optimal estimate of $Z(k)$, denoted $Z_1(k)$, is:

$$Z_1 = \frac{\langle gt^* \rangle}{\langle tt^* \rangle}, \quad (\text{C2})$$

where the angle brackets denote an average over an annulus in (k_x, k_y) space with central radius k . Conversely, if the gravity is free from noise, but the topography is noisy, one estimates $Z_3(k)$ where $t = (1/Z_3)g + n$, and:

$$Z_3 = \frac{\langle gg^* \rangle}{\langle tg^* \rangle}. \quad (\text{C3})$$

We assumed that the noise occurred in the topography, because the largest errors are in the estimation of residual topography in the absence of thickened crust, and only examined wavelengths longer than 600 km for which flexural effects are unimportant. If there is also noise in the gravity, our estimates of Z_3 will be overestimates of the true admittance. Further information about the procedure we follow is given by McKenzie & Fairhead (1997).

The method requires that the input does not contain gaps. However, if one uses topography from which regions of thickened crust have not been excluded, there is a problem if the intermediate-wavelength components of topography supported by changes in crustal thickness ($Z \sim 0$ mGal km⁻¹) coincide with topography supported by convection ($Z \sim 30$ mGal km⁻¹). This is because the overall admittance will be an underestimate of the true convective admittance (McKenzie 1994). There are therefore two options. The first is to concentrate on swells without large areas of thickened crust, and the second is to attempt to remove the topographic expression of plateaus by hand.

C1 Swells without prominent island chains

In the Pacific, we initially focussed on a swell and a trough without prominent island chains, which are marked on Figs 12(a) and (b). The results are illustrated in Figs C1(c)–(d). The admittance at wavelengths longer than 600 km has a wavelength-independent value of approximately 30 ± 5 mGal km⁻¹, which is consistent with the high correlations in Table A1. The coherence over both features is between 0.4–0.5.

In the Northwest Atlantic, we estimated Z_3 in the box marked on Figs 12(e)–(f), using both the observed and residual gravity fields as input. The error bars in Fig. 7(d) are relatively large, and we repeated the procedure using the solid curve in Fig. 7(b) to calculate the residual depths. The results are shown in Fig. C1(a). The coherence is between 0.4–0.5, and is not strongly affected by the choice of observed or residual gravity, but the estimates of Z_3 are sensitive to the choice of reference depth–age curve. Nevertheless, all three sets of estimates fall in the range 30–45 mGal km⁻¹, which is slightly higher than the estimates from swells in the Pacific.

C2 Manual correction for thickened crust

In the Northeast Atlantic, we estimated Z_3 in the box marked on Figs 12(c)–(d). Because the Cape Verde islands cover only a small fraction of the swell, we simply excluded them, and then used the GMT algorithm `surface` (Smith & Wessel 1990; Wessel & Smith 1998) with $T = 1$ to fill-in the gap. The admittance is illustrated in Fig. C1(b), and has a wavelength-independent value of ~ 25 mGal km⁻¹, irrespective of whether observed or residual gravity is used. The coherence is high (between 0.85 and 0.9).

The accuracy with which one can estimate Z increases with box size (e.g. Pérez-Gussinyé *et al.* 2004), so we also estimated the long-wavelength admittance between gravity and residual topography in a very large box covering most of the central and western Pacific, which is illustrated in Fig. C2. However, in order to obtain an estimate of the admittance in the absence of thickened crust, it was necessary to level the larger plateaus manually. Our choice of which features to exclude, and how to fill-in the gaps, is discussed

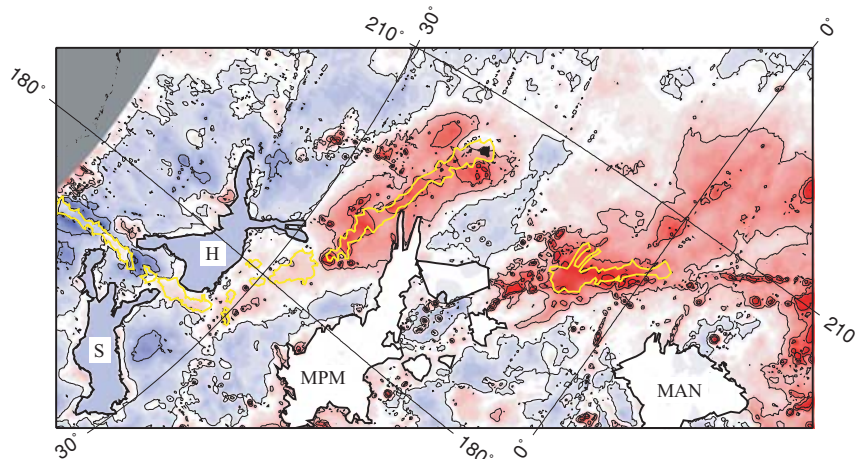


Figure C2. Residual topography in a large box covering the central and western Pacific. The admittance with gravity is plotted in Fig. C1(d). The colour scale is the same as in Fig. 12 and the contour interval is 500 m. We first excluded topography inside the regions enclosed by yellow lines, and then re-gridded the topography using the GMT algorithm `surface` with $T = 1$ (Smith & Wessel 1990; Wessel & Smith 1998). We then set the topography inside the regions enclosed by black lines to a constant value. The mid-Pacific Mountains (MPM) and Manihiki Plateau (MAN) were set to zero. The Hess Rise (H) and Shatsky Rise (S) are large regions of thickened crust which are located in a long-wavelength residual topographic and gravity low. We set them to a value of -350 m, the approximate mean for the surrounding basin. We are not concerned about the presence of small seamounts, which have almost no energy at wavelengths longer than 1000 km.

in the caption to Fig. C2. Our starting topography was the model of Smith & Sandwell (1997), and our estimate of Z_3 is illustrated in Fig. C1. The admittance is in the range 25–35 mGal km⁻¹, and varies little with wavelength. The coherence is approximately 0.7 at all wavelengths greater than 1000 km, which explains why subtracting the long-wavelength gravity field does not improve the linear correlation between the remaining gravity and topography.

APPENDIX D: AN ALTERNATIVE STRATEGY IN THE NORTH PACIFIC

One disadvantage of the approach presented in preceding sections is that the reference depth–age curves were constructed using only a small subset of the available topographic data. An alternative strategy is to subtract an estimate of the dynamic topography first, and then find the depth–age curve which minimizes the RMS misfit to all the remaining reduced topography. We used the topography of Smith & Sandwell (1997), and applied a sediment correction and the masks in Figs 2 and 4 beforehand.

We calculated the model topography as follows. First, we projected the gravity of Sandwell & Smith (1997) into Cartesian coordinates using a Lambert azimuthal equal area projection of the North Pacific. We then applied a Fast Fourier Transform (FFT), divided the FFT of the gravity by an isotropic transfer function $Z(k)$ which relates topography to gravity, and finally applied an inverse FFT in order to obtain the model topography in the space domain. At short wavelengths, $Z(k)$ is given by a model in which topography forms from the surface loading of a 10-km-thick elastic plate with a 7-km-thick crust; at long wavelengths, $Z(k)$ is a simple constant or linear function of k consistent with the estimates of $Z_3(k)$ in Fig. C1. The elastic plate thickness (T_e) was chosen to reduce noise and was a compromise between that of seafloor fabric created at the ridge ($T_e \sim 5$ km, McNutt 1979), and that of stray Western Pacific seamounts not excluded in the original processing ($T_e \sim 15$ km, Wolfe & McNutt 1991). Results for three plausible choices of long wavelength transfer function are illustrated in Fig. D1.

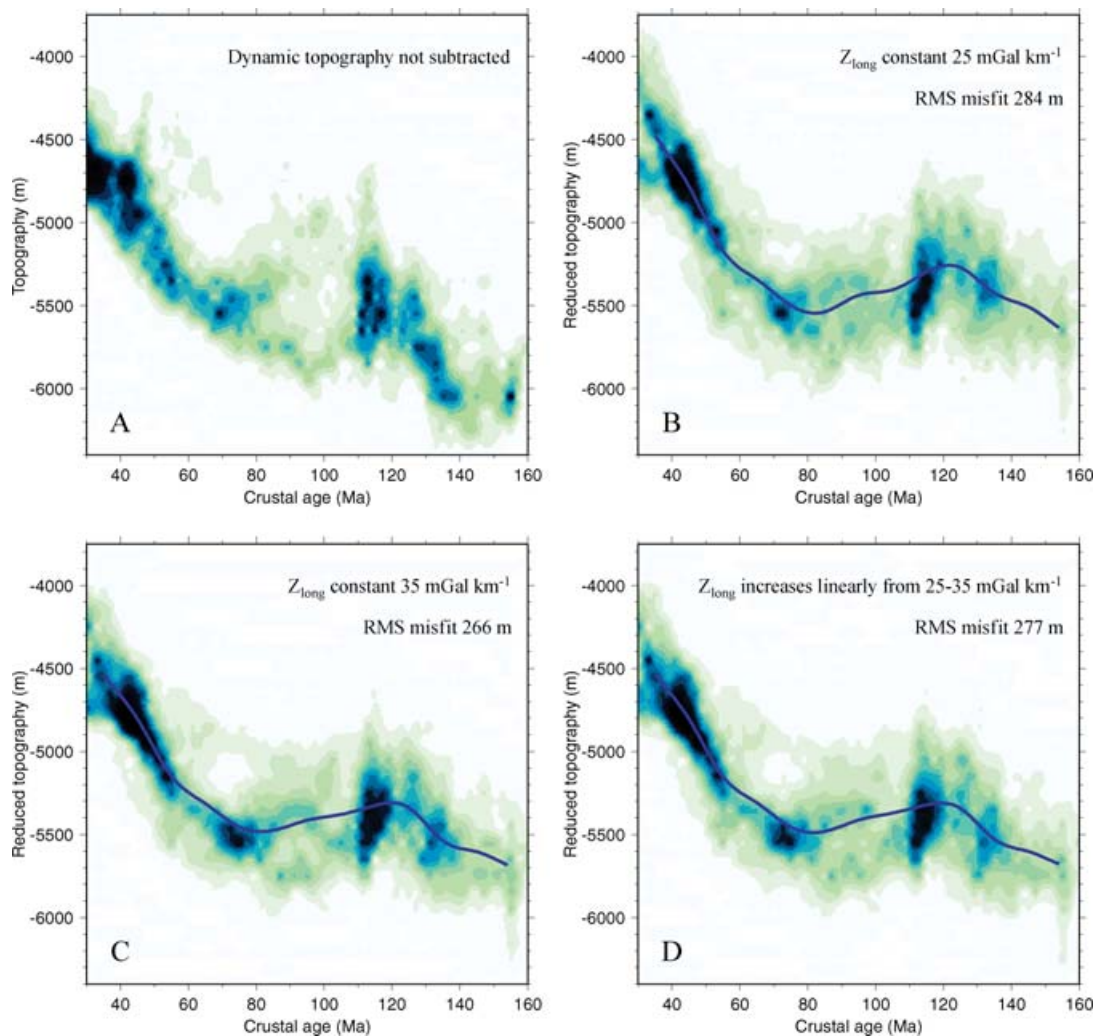


Figure D1. Gridded 2-D histograms of the depth and age in the North Pacific with a calculated dynamic topography subtracted beforehand, using sediment-corrected topography in all regions except those within the masks in Figs 2 and 4. Figures (a) is for reference and illustrates the data set without the dynamic topography subtracted. Darker colours indicate a higher density of 50 km geographical block medians within each depth–age block. The annotations in figures (b–d) indicate the nature of the transfer function between topography and gravity at long wavelengths, which was used to calculate the dynamic topography from the gravity. The thick blue line is the cubic spline, which minimizes the RMS misfit to the reduced topography. The effect of subtracting dynamic topography on the depth–age relationship is to strongly reduce the variance between the ages of 80–110 Ma, and to shallow depths between 130–160 Ma, where most of the seafloor is covered by a large negative gravity anomaly.

To calculate a depth–age curve in each case, we then used Powell’s algorithm (Press *et al.* 1992) to find 13 equally spaced depth tie-points between the ages of 30–160 Ma, for which the RMS misfit was minimized between a cubic spline interpolation through the tie points and the 50 km block-medians of the reduced topography as a function of age. The best-fitting splines are illustrated in blue in Fig. D1.

The bulge in topography as a function of age between 80–130 Ma is visible in all three plots of the reduced topography as a function of age in Fig. D1, and the RMS misfits to the best-fit splines are all in the range 265–285 m. Subtracting an estimate of the dynamic topography clearly reduces the topographic variance between 60–110 Ma, which is the region with the highest correlation between long-wavelength gravity and topography. The average depth is, however, little affected, because the gravity anomalies are almost symmetric

about zero (see Fig. 6). As expected from the observed gravity–topography correlations, a gravity–topography admittance function with a long-wavelength value of 25 mGal km^{-1} reduces the variance by a larger amount than a function with a long-wavelength value of 35 mGal km^{-1} . However, the second function reduces the topographic variance on ocean floor older than 120 Ma by a larger amount than the first function. There are two possible reasons for this. The first is that the admittance over the troughs on the old Pacific floor might be higher than the long-wavelength admittance in the mid-Pacific (which is consistent with, but not demonstrated by, Fig. C1d). The second is that the noise on the old ocean floor is associated with features which formed when T_c was larger than 10 km. More importantly, because the gravity anomalies are mostly negative over the old Pacific floor, subtracting an estimate of the dynamic topography reduces the average depth as a function of age.